Optimizing a backscatter forward operator using Sentinel-1 data over irrigated land

Sara Modanesi[1,2,4], Christian Massari[1], Alexander Gruber[2], Hans Lievens[2], Angelica Tarpanelli[1], Renato Morbidelli[3], Gabrielle J. M. De Lannoy[2]

[1]Research Institute for Geo-hydrological Protection, National Research Council, Via della Madonna Alta 126, 06128 Perugia, Italy
[2]Department of Earth and Environmental Sciences, KU Leuven, Heverlee, Belgium
[3]Dept. of Civil and Environmental Engineering of Perugia, Via G. Duranti 93, 06125 Perugia, Italy
[4]DICEA Dept. of Civil and Environmental Engineering, University of Florence, Via di S. Marta 3, 50139 Firenze, Italy

Correspondence to: Christian Massari (christian.massari@irpi.cnr.it)

Abstract. Worldwide, the amount of water used for agricultural purposes is rising and the quantification of irrigation is becoming a crucial topic. Because of the limited availability of in situ observations, an increasing number of studies is focusing on the synergistic use of models and satellite data to detect and quantify irrigation. The parameterization of irrigation in large scale Land Surface Models (LSM) is improving, but it is still hampered by the lack of information about dynamic crop rotations or the extent of irrigated areas, and the mostly unknown timing and amount of irrigation. On the other hand, remote sensing observations offer an opportunity to fill this gap as they are directly affected by, and hence potentially able to detect, irrigation. Therefore, combining LSMs and satellite information through data assimilation can offer the optimal way to quantify the water used for irrigation.

This work represents the first and necessary step towards building a reliable LSM data assimilation system which, in future analysis, will investigate the potential of high-resolution radar backscatter observations from Sentinel-1 to improve irrigation quantification. Specifically, the aim of this study is to couple the Noah-MP LSM running within the NASA Land Information System (LIS), with a backscatter observation operator for simulating unbiased backscatter predictions over irrigated lands. In this context, we first tested how well modelled Surface Soil Moisture (SSM) and vegetation estimates, with or without irrigation simulation, are able to capture the signal of aggregated 1-km Sentinel-1 backscatter observations over the Po river Valley, an important agricultural area in Northern Italy. Next, Sentinel-1 backscatter observations, together with simulated SSM and LAI, were used to optimize a Water Cloud Model (WCM) which will represent the observation operator in future data assimilation experiments. The WCM was calibrated with and without an irrigation scheme in Noah-MP, and considering two different cost functions. Results demonstrate that using an irrigation scheme provides a better calibration of the WCM, even if the simulated irrigation estimates are inaccurate. The Bayesian optimization is shown to result in the best unbiased

32 calibrated system, with minimal chance of having error cross-correlations between the model and observations. Our time series

33 analysis further confirms that Sentinel-1 is able to track the impact of human activities on the water cycle, highlighting its

34 potential to improve irrigation, soil moisture, and vegetation estimates via future data assimilation.

35 **1 INTRODUCTION**

36 Over the last century, the global water withdrawal grew 1.7 times faster than the population (FAO, 2006). This aggravates the

37 concern over the sustainability of water use as demand for agricultural uses continues to increase (Foley et al., 2011; FAO

38 AQUASTAT http://www.fao.org/nr/water/aquastat/water_use/index.stm, last access 20 May 2021). The strong impact of

39 irrigation on the global water budget is highlighted by many studies and it has been estimated that about 87% of the global fresh

40 water withdrawals have been used for agriculture (Douglas et al., 2009). Accordingly, the quantification of irrigation on a

41 regional to global scale has become a hot research topic.

42 Correctly quantifying irrigation in Earth system models can serve two purposes. On the one hand, it can help improve water

43 management (Le Page et al., 2020, Bretreger et al., 2020), on the other hand, it allows to quantitatively assess its effects on the

44 terrestrial water, carbon and energy cycles (Haddeland et al., 2007; Breña-Naranjo et al., 2014; Hu et al., 2016; Qian et al. 2020).

45 Indeed, results of large-scale irrigation studies using land surface models (LSMs) have demonstrated that irrigation increases

46 soil moisture and evapotranspiration (ET), and consequently latent heat flux with a decrease in sensible heat flux (i.e., Badger

47 & Dirmeyer, 2015; Lawston et al., 2015; Ozdogan et al., 2010b).

48 Despite the significant impact of irrigation on the water and energy cycles, its simulation within LSMs is not yet common

49 practice (Girotto et al., 2017). In earlier studies, attempts to simulate irrigation in LSMs have relied on different

50 parameterizations of well-known irrigation systems (like sprinkler, flood, and drip systems; Ozdogan et al., 2010b; Evans and

51 Zaitchik, 2008), making simplifying assumptions. For instance, in Ozdogan et al. (2010b) irrigation water is not withdrawn from

52 a source (such as a river) but instead added as fictitious rainfall. In contrast, Nie et al. (2018) accounted for source water

53 partitioning, albeit only partially, by considering groundwater irrigation. Irrigation is normally applied when soil moisture drops

54 below a user-defined threshold (Ozdogan et al. 2010b), typically dependent on the soil properties obtained via soil texture maps.

55 Moreover, LSMs equipped with irrigation schemes need to be provided with auxiliary information about crop types and whether

56 or not the crops are irrigated. This is because different crop types are characterized by different rooting depths, which means

57 they require more or less water to restore root zone field capacity. This information is normally gathered from static maps derived

58 from statistical analysis and/or remote sensing (Ozdogan et al., 2010b; Monfreda et al., 2008; Salmon et al., 2015) collected

59 during specific historical periods which are normally different to the desired period of analysis. It is thus clear that the modelling

60 of irrigation is subject to many simplifying assumptions, which span from neglecting the year-to-year crop variability and the

61 irrigation system used to the definition of irrigation application times based on water availability and crop conditions rather than

62 actual farmer decisions.

Remote sensing (RS) technologies offer the opportunity to observe directly the Earth surface and its changes, and hence are potentially able to monitor irrigated lands worldwide (Ambika et al., 2016; Gao et al., 2018; Bousbih et al., 2018; Bazzi et al., 2019; Le Page et al., 2020; Dari et al., 2020). In the last decade, some authors used visible and near infrared RS observations jointly with in situ data collected from inventories to map areas equipped for irrigation (Ambika et al., 2016; Ozdogan & Gutman, 2008). Kumar et al. (2015a) were the first to propose the use of coarse resolution satellite microwave (MW) sensors to detect irrigation. The authors compared different coarse-scale active and passive MW surface soil moisture (SSM) retrievals with SSM simulations from the Noah LSM (version 3.3; Ek et al., 2003) without activating an irrigation scheme over a continental US domain. Areas where the distributions of model and RS data sets deviated (based on a Kolmogorov-Smirnov test) were assumed to be irrigated. Even though some of the products showed a potential ability to detect irrigation, the authors concluded that the spatial mismatch between the satellite footprint and the irrigated fields, radio-frequency interference (RFI), vegetation, and topography could all deteriorate the accuracy of the results. Similar conclusions were found over the same area by Zaussinger et al. (2019) who compared coarse-scale satellite SSM products with soil moisture predictions from the Modern-Era Retrospective analysis for Research and Applications 2 (MERRA-2) in the absence of precipitation, and Escorihuela and Quintana-Seguí (2016) who additionally compared a downscaled version of the Soil Moisture and Salinity mission (SMOS) SSM to SURFEX LSM simulations. Brocca et al. (2018), Jalilvand et al. (2019) and Dari et al. (2020) used a conceptually different approach with the same coarse scale MW SSM products and estimated irrigation by directly inverting a simple water balance equation (Brocca et al. 2014).

The Copernicus Sentinel-1 satellites (Sentinel-1A and Sentinel-1B) offer a new perspective for agricultural applications, thanks to the finer spatial resolution (up to 10-20 m) of the Synthetic Aperture Radar (SAR) backscatter (σ^0) data. For instance, Gao et al. (2018) proposed an approach to map irrigated lands over the Urgell region in Catalonia (Spain), and Le Page et al. (2020) proposed a methodology to detect irrigation timing in south-west France comparing the SSM signal at the plot scale, derived using Sentinel-1 σ^0 and NDVI from Sentinel-2 (El Hajj et al., 2017), with a water budget model forced by Sentinel-2 optical data for the detection of irrigation timing.

Despite the high potential demonstrated by RS in detecting, mapping and quantifying irrigation, the uncertainties of the satellite retrievals, the relatively low revisit time of high resolution active MW products and the too coarse spatial resolution of passive MW products with respect to the mean size of irrigated fields represent main limitations for irrigation information retrieval (Romaguera et al., 2010, La Page et al., 2020). Data assimilation (DA) could reduce some uncertainties by optimally integrating LSM estimates and RS observations. Indeed, the LSM estimates resolve processes at desired spatio-temporal scales, while the RS observations can track in a more realistic way human processes like irrigation and their interactions with the water and energy cycles. Contrasting LSM simulations with RS observations offers an opportunity to correct for unmodeled processes or missed events, such as irrigation (Kumar et al., 2015a; Girotto et al., 2017). More generally, DA of satellite-based observations has shown the potential to update soil moisture (De Lannoy & Reichle, 2016; Kolassa et al., 2017) and vegetation (Albergel et al., 2018; Kumar et al., 2020) and important impacts have been reported over agricultural areas (Kumar et al., 2020).

96   The assimilation of MW RS observations in LSMs often involves retrieval assimilation. However, assimilating retrievals (i.e.,
97   SSM or vegetation optical depth rather than MW brightness temperature or σ^0 measurements) can be problematic as the retrievals
98   may have been produced with ancillary data that are inconsistent with those used in the LSM (De Lannoy et al. 2016). This is
99   particularly true for passive MW retrievals while active MW retrievals generally rely on change detection methods that lack
100   land-specific ancillary information altogether. An alternative approach, which we follow in this study, is to directly assimilate
101   MW observations and equip the LSM with an observation operator that links land surface variables of interest (e.g., soil moisture
102   and vegetation) with RS data. This allows us to obtain consistent parameters and to reduce the chance of cross-correlated errors
103   between model states and corresponding geophysical satellite retrievals. The direct assimilation of MW observations has already
104   been demonstrated successfully for the update of soil moisture by using Tb derived from the SMOS and SMAP missions (De
105   Lannoy et al. 2016, Carrera et al., 2019, Reichle et al. 2019), as well as using radar σ^0 from ASCAT (Lievens et al., 2017b), and
106   σ^0 from Sentinel-1 in synergy with SMAP Tb (Lievens et al., 2017a). However, to our knowledge, none of these studies
107   considered the joint updating of soil moisture and vegetation, and none specifically focused on the performance over irrigated
108   areas. The σ^0 from Sentinel-1 contains information on both soil moisture (Zribi et al., 2011; Liu and Shi, 2016; Li and Wang,
109   2018; Bauer-Marschallinger et al., 2018) and vegetation (Vreugdenhil et al., 2018; Vreugdenhil et al., 2020) and assimilating
110   this data could allow us to update both soil moisture and vegetation in a land data assimilation system and, in doing so, correct
111   for missed irrigation events.

112   To that end, the LSM needs to be coupled to a backscatter forward model as an observation operator. Different SAR σ^0 models
113   have been proposed to simulate the backscattering contributions of soil and vegetation (Attema & Ulaby, 1978; Oh, 2004; Zribi
114   et al., 2005; Bai et al., 2015; Baghdadi et al., 2017). Most commonly used, the Water Cloud Model (WCM hereafter) developed
115   by Attema and Ulaby (1978) is a σ^0 model that represents the vegetation canopy as a homogeneous cloud containing randomly
116   distributed water droplets. In order to use the WCM as the forward operator in a σ^0 data assimilation system, it first needs to be
117   calibrated to account for biases between the LSM simulations and the satellite observations. However, calibrating a WCM to
118   simulate σ^0 over irrigated areas, is not a straightforward process and it represents a key research problem if the same σ^0 signal is
119   used for the calibration of WCM parameters and later for assimilation and state updating. In fact, if the objective is to assimilate
120   radar σ^0 to realistically inform the model about irrigation applications, the WCM parameters have to maintain a certain degree
121   of independence from the irrigation signal contained in the observed σ^0 as otherwise the assumption of uncorrelated errors
122   between model and observations typical of classical Bayesian-based filters is violated. More specifically, if the LSM provides
123   unrealistic simulations as input (i.e., absence of irrigation), then the WCM calibration with observed σ^0 would compensate for
124   this bias. This would in turn lead to a biased backscatter model with undesirable calibrated parameters for the subsequent data
125   assimilation experiments. Therefore, different strategies can be adopted, for instance calibrating the model during non-irrigated
126   periods or over non-irrigated areas, or equipping the LSM with an irrigation module that makes the WCM less constrained by
127   inconsistencies between simulated and observed σ^0 during irrigation periods. The efficacy of these strategies has so far never
128   been explored.

129 The main objective of this study is to simulate radar σ^0 using a LSM coupled with a WCM and to provide solutions and
130 recommendations for the optimization of the WCM as an observation operator. This is a major stepping-stone towards the
131 development of a reliable system for the assimilation of high-resolution Sentinel-1 σ^0 observations over irrigated areas.
132 Additionally, we aim at:

    1) 133 testing the ability of a sprinkler irrigation system coupled with a LSM to simulate irrigation so as to highlight the
134   potential and limitations of such a tool to optimize a backscatter forward operator over heavily irrigated areas;

    2) 135 demonstrating that Sentinel-1 σ^0 observations contain valuable information to improve both SM and vegetation
136   predictions over irrigated land (i.e., soil moisture and vegetation consistent with human alterations in the water
137   cycle due to intensive irrigation).

138 The analysis is carried out over the Po river valley, one of the most important agricultural areas in Italy and also one of the more
139 intensively irrigated areas in Europe (water withdrawal in the Po basin is estimated to be 20.5 billion m^3/year, of which 16.5
140 billion of m^3/year is withdrawn for irrigation; Po River Watershed Authority, 2006). We use the Noah-MP v.3.6 LSM (Noah-
141 MP hereafter) as part of the NASA Land Information System (LIS) framework together with the WCM from Attema and Ulaby
142 (1978) for the simulation of both σ^0 vertical send and receive (VV) and vertical send and horizontal receive (VH) polarization.
143 Level-1 Sentinel-1 σ^0 observations are used to calibrate the WCM at 1-km resolution, using simulated SSM and Leaf Area Index
144 (LAI) estimates from Noah-MP. The WCM is calibrated for a total of four calibration experiments for each polarization: 1) with
145 or without activating an irrigation scheme within Noah-MP; and, 2) considering two different cost functions. Specifically, we
146 want to demonstrate that activating an -even poor- irrigation scheme is needed to obtain long-term unbiased σ^0 simulations and
147 uncorrelated errors between the WCM and Sentinel-1 and that the calibration process can be sensitive to different cost functions.
148 The manuscript is organized as follows. Section 2 provides information on the study area, the selected datasets, and methods
149 used for our analysis. Specifically, Sections 2.3 and 2.4 provide a detailed description of the Noah-MP LSM and the WCM.
150 Section 2.5 describes the cost functions used for the WCM calibration while Section 2.6 is a description of the experimental set-
151 up designed for the calibration. Finally, Section 2.7 provides insights on the Noah-MP and WCM evaluations. Section 3 presents
152 the results, with an assessment of the Noah-MP evaluation, both regional (Section 3.1) and over the test sites (Section 3.2). The
153 WCM calibration and evaluation results are described in Sections 3.3 and 3.4, respectively. We provide discussion in Section 4
154 while conclusions are reported in Section 5.

155 **2 DATA AND METHODS**

156 **2.1 Study area and in situ data**

157 The analysis was carried out over an area of 24,000 km^2 located within the Po river valley, one of the most important agricultural
158 areas in Europe (Figure 1, left-bottom corner: 44°N, 10.5°W; top-right corner: 45.5°N, 12.2°W). The Po river valley is part of
159 the Po river basin district (~74,000 km^2), a mountain-fed catchment which extends from the Alps in the West, to the Adriatic
160 Sea in the East. The Po district is one of the eight districts mentioned in the Water Framework Directive (WFD, 2000) initiated

by the European Commission and has been hit by seasonal drought events which impacted all water use sectors, in particular agriculture (Strosser et al., 2012). The water assessment and impact evaluation of human activities over the Po river valley is thus a topic of major interest, considering the significant requirements from the agricultural management sector.

According to the Köppen-Geiger climate classes (Peel et al., 2007) the study area is classified as "Cfa" (temperate climate, without dry season and with hot summers). From a geographical point of view, the Po river flows from the west to the east, splitting the area of interest in northern and southern areas, respectively. North of the Po river, the agricultural plain area can be additionally subdivided into the Veneto region to the east and the Lombardy region to the west (Figure 1). Lombardy lands have a high water availability, thanks to the presence of several Alpine lakes and reservoirs (Musolino et al., 2017), as does the Veneto region. Wine cultivation plays an important role, especially in the Garda Lake surroundings (located to the north-west side of the study area). In the south, the Emilia Romagna region is an agricultural as well as urbanized-industrialized area. Compared to Lombardy and Veneto, Emilia Romagna is much poorer both in water availability and storage capacity, but its irrigation system is considered the most technologically advanced and efficient in the Po river basin (Musolino et al., 2017). Specifically, it hosts the Canale Emiliano Romagnolo (CER, https://consorziocer.it/it/, last access 20 May 2021), one of the most important Italian hydraulic systems for agricultural water supply. The main crops in the study region include general summer and winter crops, orchards (i.e., peach, pear, kiwi), olive groves, and vineyards (https://sites.google.com/drive.arpae.it/servizio-climatico-icolt/home, last access 20 May 2021). The plain area is surrounded by a forested hilly and mountainous area of the Tuscan-Emilian Appennine to the south/south-west.

In situ data were collected over two test sites, located in the Emilia Romagna region:

- For an analysis at plot scale we selected the Budrio test site (Figure 1a), an experimental farm managed by the CER authority which includes two plots of 0.39-0.49 ha. The main crops are maize for field 1 (in yellow) and tomatoes in field 2 (red colour). Daily irrigation data, in mm, were collected for the summer 2015-2016 over field 1, whereas daily irrigation water amounts were collected for the summer 2017 over field 2. Additionally, for field 2, hourly in situ soil moisture data, aggregated here at daily scale, were made available from the Department of Physics and Earth Science of the University of Ferrara. The soil moisture data were derived from an innovative Proximal Gamma-Ray (PGR SM hereafter; Filippucci et al., 2020, Strati et al., 2018) station, equipped with a 1L NaI(Tl) detector placed at 2.25 m above the ground and a commercial agro-meteorological station (MeteoSense 2.0, Netsen; Strati et al., 2018). The PGR is a nuclear non-invasive and non-contact technique, which allows to overcome the issue connected to in situ point measurements, probing soil moisture with a field scale footprint ($\sim 10^4$ m^2) up to a depth of 30 ~ cm. The quantification of PGR soil moisture is derived from measurements of gamma signals emitted by the decay of ^{40}K, which is extremely sensitive to different soil water contents in agricultural soils (for more information on the PGR soil moisture deriving procedure the reader can refer to Baldoncini et al., 2019). Finally, daily rainfall data were collected from the national rainfall network managed by the Department of Civil and Environmental Protection (DPC) of Italy, for the irrigated periods.

194   ● The second test site (Figure 1b) is located around the city of Faenza (hereafter Faenza test site) and has a total extent
195   of 1051 ha, consisting of two fields which allow an analysis at the small-district spatial scale. The first one is called
196   San Silvestro (290 ha) and it is located north of the city. The second one is called Formellino (760 ha), located east
197   to the San Silvestro field and north-east to the city of Faenza. Fruit trees are prevalent on the fields; in particular, pear
198   trees and kiwi dominate the area. The water used for irrigation was provided by CER, at hourly time scale and in mm,
199   for the 2-years time period 2016-2017. Daily rainfall data were collected from the national rainfall network managed
200   from the DPC.

2.2 Sentinel-1 σ^0 and reference remote sensing products

202 The Copernicus-ESA Sentinel-1 σ^0 observations were used in this study for the calibration of the WCM. The Sentinel-1
203 constellation consists of two satellites, Sentinel-1A and Sentinel-1B, launched in 2014 and 2016, respectively. Each satellite
204 carries a Synthetic Aperture Radar (SAR) operating at C-band (5.4 GHz) in the microwave portion of the electromagnetic
205 spectrum. The processing of the ground-range detected (GRD) Interferometric Wide Swath (IW) observations in VV- and VH-
206 polarization was done using Google Earth Engine's Python interface and included standard techniques: precise orbit file
207 application, border noise removal, thermal noise removal, radiometric calibration, and range-Doppler terrain correction.
208 Furthermore, the σ^0 observations acquired at 5×20 m^2 resolution were aggregated and projected on the 1 km Equal Area Scalable
209 Earth version 2 (EASE-2) grid (Brodzik et al., 2012). After applying an orbit bias-correction (Lievens et al., 2019), the
210 observations from different orbits, either from Sentinel-1A or -1B and ascending or descending tracks, were combined at the
211 daily time-scale.

212 Additionally, RS observations were used for the evaluation of the SSM and LAI simulated in Noah-MP LSM for the period 31
213 March 2015- December 2019:

214   ● The NASA Soil Moisture Active Passive (SMAP; Entekhabi et al., 2010) is an orbiting observatory launched in
215   January 2015 carrying two instruments: a SAR which suffered a failure in early July 2015, and a radiometer measuring
216   Tb at L-band, with a native spatial resolution of 40 km, a revisit time of 2–3 days, and ascending and descending
217   overpasses at 6:00 PM and 6:00 AM (local time), respectively. For this study, the 9-km SMAP Enhanced Level-2
218   SSM version 4 (0-5 cm; SMAP L2 hereafter) product was used (O'Neill et al., 2020; Chan et al., 2018). The product
219   is derived from SMAP Level-1B (L1B) interpolated antenna temperatures using the Backus-Gilbert optimal
220   interpolation technique. Both ascending and descending tracks were collected.
221   ● The Metop ASCAT SSM Climate Data Records (CDR) H115 and its extension H116 are provided by the European
222   Organization for the Exploitation of Meteorological Satellites (EUMETSAT) Support to Operational Hydrology and
223   Water Management (H SAF; http://hsaf.meteoam.it/, last access 20 May 2021). The SSM is retrieved from σ^0 using
224   a change detection algorithm (Wagner et al., 2013), and is characterized by a spatial sampling of 12.5 km and a
225   temporal resolution of one to two observations per day, depending on the latitude.

226   ●   The PROBA-V LAI is derived from the PROBA-V satellite mission (Francois et al., 2014; Dierckx et al., 2014) and

227   provided by the Copernicus Global Land Service programme (CGLS, https://land.copernicus.eu/global/). The CGLS

228   product at 1 km spatial resolution and 10-day (dekadal) temporal resolution is developed based on the work by Verger

229   et al. (2014).

230 In order to compare Noah-MP simulations and reference data at the same spatial resolution, Sentinel-1 observations (σ^0-VV and

231 -VH), as well as ASCAT SSM, SMAP L2 SSM and PROBA-V LAI were extracted over the study domain (left-bottom corner:

232 44°N, 10.5°W; top-right corner: 45.5°N, 12.2°W) and re-gridded over the LIS grid domain (0.01°) using the nearest-neighbour

233 approach.

2.3 Land surface and irrigation modelling

2.3.1 Noah-MP v.3.6

236 The analysis was carried out using the Noah-MP (Niu et al., 2011) LSM, running within NASA's LIS 7.2 version (Kumar et al.,

237 2008). LIS is a software framework for terrestrial hydrology modelling and DA, which supports different LSMs that can be

238 conditioned on multiple remote sensing products from active and/or passive microwave sensors. The Noah-MP LSM, which

239 was chosen for this study, is an evolution of the baseline Noah LSM (Mahrt and Ek, 1984; Chen et al., 1996; Chen and Dudhia,

240 2001) wherein main improvements and augmentations are: 1) the presence of four soil layers; 2) up to three snow layers; 3) one

241 canopy layer which allows to dynamically simulate the vegetation and to compute separately the ground surface temperature; 4)

242 a two-stream radiation transfer scheme based on the canopy layer sub-grid scheme; 5) a Ball-Berry type stomatal resistance

243 scheme; 6) and finally, a simple groundwater model with a TOPMODEL-based runoff scheme (Niu et al., 2005, 2007). The

244 model was set up selecting four soil layers at depths 0–10, 10–40, 40–100 and 100–200 cm, a dynamic vegetation model with a

245 Ball-Berry type canopy stomatal resistance model (Ball et al., 1987), and TOPMODEL-based runoff.

246 The parameterization followed the recommended options provided in the LIS documentation

247 (https://modelingguru.nasa.gov/docs/DOC-2634). A model time step of 15 minutes and a 6 hours output interval were selected

248 together with a spatial resolution of 0.01°. The meteorological forcings used for running Noah-MP LSM were obtained from

249 MERRA-2 (Gelaro et al. 2017). The MERRA-2 original spatial resolution of 0.5°x0.625° was re-mapped to 0.01° through

250 bilinear interpolation. Land model data and parameters were pre-processed and adapted to the LIS longitude/latitude projection

251 using the Land Surface Data Toolkit (LDT; Arsenault et al., 2018) in order to run Noah-MP at the chosen spatial resolution.

252 For this study, the default LIS Land Cover (LC) map from the University of Maryland (UMD) global land cover product (Hansen

253 et al., 2000) based on the Advanced Very High Resolution Radiometer (AVHRR) data was replaced with the 2015 global LC

254 map, available from the CGLS at 100 m spatial resolution (Buchhorn et al., 2020; available at

255 https://land.copernicus.eu/global/products/lc , last access 20 May 2021). The CGLS provides Dynamic Land Cover Layers at

256 100 m spatial resolution (CGLS-LC100), obtained by combining information derived from the vegetation instrument on board

257 the PROBA-V satellite, a database of high-quality LC reference sites, and several ancillary datasets. For a more detailed

explanation of the LC maps generation process we refer to the Algorithm Theoretical Basis Document (ATBD; Buchorn et al., 2020). The 23 classes of the PROBA-V LC map were reclassified to the 14 classes used in the UMD-AVHRR classification supported by LIS. Additionally, the LC map was regridded at 0.01° (Figure 2a) by identifying the most representative class over each LIS grid cell. For additional information on the reclassification process, we refer the reader to Table S1 in the Supplementary Material section. Similarly, the default FAO Soil Map (FAO Soil Map of the World, 1971) was replaced by the Harmonized Soil World Database (HWSD v1.21, 1 km; Figure 2b) and mapped to 5 soil classes over the study region. Other model pre-processed parameters inputs were: i) the Shuttle Radar Topography Mission elevation data (SRTM30, 30 m spatial resolution); 2) climatological global Greenness Vegetation Fraction (GVF) data (0.144°; Gutman and Ignatov, 1998) derived from 5 years (1985-1989) of normalized difference vegetation index (NDVI) data from the AVHRR (Miller et al., 2006); 3) a snow-free albedo and a Noah-specific maximum snow albedo product from NCEP (original resolution 1° and regridded); and finally, 4) soil, vegetation, and other general parameter tables for Noah-MP from the LIS official Data Portal (https://portal.nccs.nasa.gov/lisdata_pub/data/, last access 20 May 2021).

2.3.2 Irrigation modelling

The ability of Noah-MP to dynamically simulate the vegetation and the option to activate irrigation are particularly important considering an extensively irrigated area such as the Po river valley. Indeed, in a recent study by Nie et al. (2018), Noah-MP was coupled with a sprinkler irrigation scheme (Ozdogan et al., 2010b) (where irrigation is applied as supplementary rainfall), which requires three pieces of information:

- the irrigation location, only occurring over potentially irrigated croplands (expanding over grassland if the intensity exceeds the gridcell's total crop fraction). This information is extracted from a LC map associated with an additional dataset providing information on the percent of irrigated area per grid cell. In this study, the reclassified PROBA-V LC map was coupled with the information contained in the 500 m Global Rain-fed, Irrigated and Paddy Croplands data set (GRIPC; Salmon et al., 2015);

- the timing of irrigation, which is determined by checking the start and end of the growing season based on a GVF threshold, separately at each grid cell. Following Ozdogan et al.(2010b), we set this threshold to 40% of the GVF;

- the amount of water used for irrigation. This quantity is derived from the root zone soil moisture (RZSM) availability (MA) as MA=(RZSM-SM_{WP})/(SM_{FC}-SM_{WP}) where RZSM is the current RZSM, SM_{WP} is the wilting point, and SM_{FC} is the field capacity. When the MA falls below a user-defined threshold, irrigation is triggered and the quantity is defined by calculating the amount of irrigation needed to raise the RZSM to the SM_{FC}. For this study, the MA threshold was defined as the 50% of SM_{FC} as in Ozdogan et al. (2010b). MA is calculated at each time step but the irrigation is only applied between 06:00 and 10:00 LT. Following Ozdogan et al. (2010b), this time frame is typically chosen by farmers to reduce evaporative losses. In this context, the maximum rooting depth becomes a crucial information to compute the amount of irrigation water. This information is related to an assigned crop type, cultivated over the study area, through a maximum rooting depth table. Considering the high crop variability over the Po river valley as well as the lack of high

resolution dynamic crop maps for the entire study area, a generic crop type with 1 m root depth was selected for the irrigation simulations. The reference rooting depth was verified to be feasible over the study area based on the European Soil Data Centre (ESDAC, available at https://esdac.jrc.ec.europa.eu/content/european-soil-database-derived-data, last access 20 May 2021) rooting depths map (Figure S1 in the Supplementary Material).

2.4 Water Cloud Model

The WCM allows to simulate the top-of-vegetation σ^0 as a function of SSM and vegetation, using empirical fitting parameters. σ^0 is modeled as the sum of the backscatter from the vegetation (σ^0_{veg}, in dB) and from the bare soil (σ^0_{soil}, in dB), attenuated by the t^2 coefficient that describes the two-way attenuation from the vegetation layer. Scattering interactions between the ground and the vegetation are not accounted for. As reported in Baghdadi et al. (2018), for a given polarization pq (i.e., VV and VH), the WCM can be written as follows:

$$\sigma^0_{pq} = \sigma^0_{veg,pq} + t^2_{pq}\sigma^0_{soil,pq} \tag{1}$$

where:

$$\sigma^0_{veg,pq} = A_{pq}V_1 cos\theta(1 - t^2_{pq}) \tag{2}$$

$$t^2_{pq} = exp(\frac{-2B_{pq}V_2}{cos\theta}) \tag{3}$$

$$\sigma^0_{soil,pq} = C_{pq} + D_{pq} \cdot SSM \tag{4}$$

Equations 2 and 3 describe the vegetation-related terms. V_1 and V_2 represent two bulk vegetation descriptors, the first one accounting for the direct vegetation σ^0, and the second one representing the attenuation. A_{pq}[-] and B_{pq}[-] are the two related fitting parameters. Common vegetation descriptors used in previous studies are the Vegetation Water Content (VWC, Paloscia et al., 2013), the NDVI (El Hajj et al., 2016; Li and Wang, 2018) and LAI (Kumar et al., 2015b; Bai and He, 2015), while θ represents the incidence angle, which is assumed to be 37° for Sentinel-1. Following previous studies (see Lievens et al, 2017b; Baghdadi et al. 2017; Li and Wang, 2018) we assumed $V_1=V_2$ represented by the dynamically simulated LAI vegetation descriptor.

Equation 4 describes the soil-related term. Following the work by Lievens et al. (2017b), the σ^0_{soil} can be described, in a simple linear approach, as a function of the SSM. There are several semi-empirical models (e.g., the Oh model; Oh et al., 1992) or theoretical models (e.g., the Integral Equation Model (IEM), Fung, 1994) which describe the scattering processes related to the bare soil, but their application as a forward operator coupled to a LSM has two main limitations: the first one lies in the difficulty in retrieving soil roughness values over extended reference areas required to parameterize these models; the second one is their saturation of σ^0 in moist conditions which causes low variability in simulated σ^0 if the LSM soil moisture

320 simulations are biased wet (for more information see Lievens et al., 2017b). Those limitations justify the use of a linear fitted

321 approach. In Equation 4, the C and D parameters (here fitted in dB and dB/m^3/m^3, respectively, but σ^0_{soil} is transformed back

322 to the linear scale in Equation 1) describe the linear relation between $\sigma^0_{soil,pq}$ and SSM. Those parameters, as well as A and

323 B (-), need to be calibrated separately for each polarization.

2.5 Calibration algorithms

325 We considered two different objective functions to optimize the A, B, C and D parameters:

- 326 a Bayesian solution, which minimizes the Sum of Squared Errors (SSE) between σ^0 observations from Sentinel-1 and
  327 WCM simulations. The SSE Bayesian calibration solution aims at identifying the optimal parameter vector $\boldsymbol{\alpha}$ which
  328 maximizes the probability of the resulting σ^0 simulations $p(\hat{y}^-) = p(\hat{y}^-|\alpha)p(\alpha)$, where $p(\alpha)$ is the prior parameter
  329 distribution and $p(\hat{y}^-|\alpha)$ is the likelihood. Starting from the assumption of an independent and identically distributed
  330 normal error model, the posterior probability can be maximized by maximizing:

$$p(\hat{y}^-|\alpha)p(\alpha) = \prod_i^{N_i}\left\{\frac{1}{s_i\sqrt{2\pi}}exp\left(-\frac{(\hat{y}-\hat{y}^-)_i^2}{2s_i^2}\right)\right\} \cdot \prod_j^{N_\alpha}\left\{\frac{1}{s_j\sqrt{2\pi}}exp\left(-\frac{(\alpha_0-\alpha)_j^2}{2s_j^2}\right)\right\} \qquad (5)$$

332 i.e., the combination of the likelihood and a prior parameter constraint. The latter helps in reducing problems of
333 equifinality. In Equation (5), $\hat{y}$ represents the observed σ^0, $\hat{y}^-$ is the simulated σ^0, i is the timestep and s_i is the standard
334 deviation of the residual differences between the observed and simulated σ^0 values for N_i time steps. N_α is the number
335 of parameters to be calibrated, α_0 is the prior parameter constraint and the parameter deviation is limited by s_j^2, the
336 variance of a uniform distribution $s_j^2 = \left(\alpha_{max,j} - \alpha_{min,j}\right)^2/12$ with determined boundaries of the parameters
337 [$\alpha_{min},\alpha_{max}$]. The maximum likelihood solution is found by minimizing the following cost function J:

$$J = \sum_i^{N_i}\left\{ln(s_i) + \frac{(\hat{y}-\hat{y}^-)_i^2}{2s_i^2}\right\} + \sum_j^{N_\alpha}\left\{\frac{(\alpha_0-\alpha)_j^2}{2s_j^2}\right\} = J_0 + J_\alpha \qquad (6)$$

339 where s_i is assumed to be constant in time and represented by a target accuracy of 1 dB, leaving the SSE in the first
340 term of J_0 to minimize. The second term (J_α) constrains the optimal solution by avoiding strong deviations from initial
341 parameter guesses.

- 342 a solution that maximizes the Kling-Gupta Efficiency (KGE; Gupta et al., 2009). Even though this objective function
  343 does not ensure Bayesian optimality, it is a widely used metric which could help to better tune the dynamic σ^0
  344 behaviour:

$$KGE = 1 - \sqrt{(r-1)^2 + \left(\frac{<\hat{y}^->}{<\hat{y}>} - 1\right)^2 + \left(\frac{s[\hat{y}^-]/<\hat{y}^->}{s[\hat{y}]/<\hat{y}>} - 1\right)^2} \qquad (7)$$

345

346   The *KGE* formulation embeds three terms: 1) the first term accounting for the Pearson Correlation (Pearson-R)

347   between the observed ($\hat{y}$) and simulated ($\hat{y}^-$) σ^0 time series; 2) a second term accounting for the bias, where the long-

348   term mean is represented as <.>; and finally, 3) a term accounting for the variability of the simulated and observed

349   signal through the use of the standard deviation s[.]. *KGE* = 1 indicates a perfect agreement between simulations and

350   observations. Note that *KGE* redistributes the weight of the bias, variance and correlation components, compared to

351   *J* in Equation 6, which can help in reducing differences between simulated and observed σ^0 also in terms of temporal

352   dynamics during the calibration. On the other hand, in the *KGE* cost function parameters are not constrained by prior

353   values α_0. This could possibly result in overfitting and a larger prediction uncertainty.

354 The Particle Swarm Optimization (PSO; Kennedy and Eberhart, 1995) was used to minimize *J* and maximize *KGE*. For our

355 case study the PSO parameters were set as in De Lannoy et al. (2013).

356 **2.6 Experimental setup**

357 An optimal DA system requires long-term unbiased σ^0 simulations (with respect to the assimilated observations). The risk,

358 over an intensively irrigated area, is that an unmodelled irrigation signal would manifest itself as a predominant bias in the σ^0

359 simulations. The calibration would then inadvertently correct for this supposed bias (i.e., the irrigation signal), thus preventing

360 the DA system from propagating the missing irrigation signal from the observations into the model. Even though existing

361 irrigation schemes are evidently unrealistic and inaccurate, we conjecture that using such a scheme when calibrating the WCM

362 will more likely yield optimal WCM parameters than when neglecting irrigation.

363 To that end, we considered two different experiment lines (referred to as *Natural* and *Irrigation,* respectively) that produced a

364 total of eight different σ^0 simulation runs (see Figure 3). The *Natural* experiment line differs from the *Irrigation* line by the

365 activation of an irrigation module in Noah-MP, and both are subjected to the calibration algorithms described in Section 2.5.

366 The *Natural* line was used as a diagnostic experiment against which to compare *Irrigation,* which, according to our initial

367 hypothesis, should minimize the impact of the irrigation signal contained in the σ^0 observations on WCM parameters.

368 As a first step, a model spin up was performed, starting in January 1982 and ending in December 2014. Then, a study period

369 from January 2015 to December 2019 was selected for the different model runs based on the availability of the processed

370 Sentinel-1 σ^0 and reference irrigation data (see Sections 2.1 and 2.2). Daily surface model and irrigation outputs were produced.

371 Considering that the main source of irrigation in the Po river valley is related to surface water abstraction, the sprinkler

372 irrigation scheme did not account for groundwater withdrawals (see Nie et al., 2018).

373 The A, B, C, and D parameters of the WCM (see section 2.4) were fitted separately to Sentinel-1 σ^0 VV and VH observations,

374 during the period January 2017 - December 2019. Following previous literature (Lievens et al., 2017b; De Lannoy et al., 2014;

375 De Lannoy et al., 2013), we performed a grid cell-based calibration to account for the spatial variability in the simulated and

376   observed σ^0 signals that stems from specific features within the observed footprints as well as from the soil and vegetation

377   parameterization of Noah-MP. Both the calibration using the SSE with prior constraint (Bayesian J) and the KGE were applied

378   to the *Natural* and *Irrigation* runs providing eight different experiments named *J-VV Natural*, *J-VH Natural*, *J-VV Irrigation*,

379   *J-VH Irrigation*, *KGE-VV Natural*, *KGE-VH Natural*, *KGE-VV Irrigation* and *KGE-VH Irrigation.*

380   Lower and upper boundaries as well as prior guess values of the WCM parameters were defined based on the work of Lievens

381   et al. (2017b) and on a sensitivity analysis (not shown here). The selected values are displayed in Table 1. Finally, it should be

382   noted that all the calibration experiments were realized by considering daily values of σ^0 simulations and observations.

383 **Table 1: Lower boundaries (LB), upper boundaries (UB), and prior guess values of the WCM parameters for both VV and VH**
384 **polarization**

	A-VV[-]	A-VH[-]	B-VV[-]	B-VH[-]	C-VV[dB]	C-VH[dB]	D-VV[dB/m³/m³]	D-VH[dB/m³/m³]
UB	0.4	0.4	0.4	0.4	-10	-10	80	80
LB	0	0	0	0	-35	-35	15	15
GUESS	0	0	0	0	-20	-30	40	40

385

386 **2.7 Noah-MP LSM and WCM evaluations**

387   The validation aims at i) evaluating the performance of Noah-MP in simulating irrigation, soil moisture, and vegetation and

388   the ability of the WCM to simulate radar σ^0, and ii) unveiling the information about irrigation contained in Sentinel-1 radar σ^0

389   in order to assess its potential to improve both soil moisture and vegetation representation within Noah-MP.

390   The evaluation was carried out on both the regional scale (i.e., over the entire study area) and on the two selected sites, Faenza

391   (small-district scale) and Budrio (plot scale), where irrigation data were available. Considering the lack of benchmark data for

392   irrigation evaluation (Foster et al., 2020) we decided to use in situ data for the small Budrio fields spatial scale (i.e., 0.45-049

393   Ha) even though model simulations are made at a much coarser resolution (i.e., ~1 km). We are aware that differences in

394   spatial scale can increase the uncertainty of our evaluation, but 0.01° LSM spatial resolution is still a good compromise for an

395   analysis at regional, small-district and plot scale. Additionally, limitations are partly reduced by the low chance of including

396   non-irrigated fields within the 1 km LIS grid cells within the Po River Valley, as the latter is almost entirely irrigated (Salmon

397   et al., 2015). We compared Noah-MP (with and without using the irrigation module) SSM and LAI simulations with satellite

398   SSM from ASCAT and SMAP, and LAI from PROBA-V, respectively, during the period 2015-2019. Furthermore, these land

399   surface simulations were compared to Sentinel-1 σ^0 to understand how much of the SSM and LAI signal was captured by

400   Sentinel-1.

As the irrigation timing is often driven by the stakeholders' turns to withdraw water and by water availability rather than by the conditions of the soil and crops themselves, the comparisons between simulated SSM and satellite SSM were carried out by aggregating the two variables over a bi-weekly time window. On the other hand, the LAI from Noah-MP was aggregated to ten-daily values in order to match the dekadal PROBA-V LAI values. We used the Pearson-R for SSM and LAI evaluation. For SSM, we also computed the Root Mean Square Error (RMSE), calculated considering the original temporal resolution of the satellite products, while for LAI, we also tested the ratio bias, i.e., the ratio between the long-term mean of the simulations and the long-term mean of observations. In particular, this additional score for LAI was used to provide a further evaluation of the ability of the Noah-MP to simulate crop phenology during the irrigated vs non-irrigated periods so as to not rely solely on the evaluation of temporal dynamics, which, due to the uncertainty in the Noah-MP crop type parameterization, could be affected by time shifts in the LAI climatology. This parameterization uncertainty comes from the lack of knowledge of the spatial crop type information and is difficult to be reduced without additional information. Our assumption is that radar σ^0 assimilation can also correct for this with future data assimilation.

Following Vreugdenhil et al. (2018) and Vreugdenhil et al. (2020), Noah-MP LAI and PROBA-V LAI were also compared with the Sentinel-1 σ^0 VH/ σ^0 VV cross ratio (CR), which was demonstrated to have a high agreement with the vegetation signal. Though the σ^0 VH was demonstrated to increase with the vegetation signal (Macelloni et al., 2001), the CR will be more sensitive to vegetation changes as the ratio is less sensitive to changes in soil moisture and soil-vegetation interaction (Veloso et al., 2017; Vreugdenhil et al., 2020).

To evaluate WCM simulations, we used bi-weekly values of σ^0 simulations and observations considering a two-years period independent from the calibration period: 2015-2016. Statistical metrics such as grid-based temporal Pearson-R, KGE, and bias were calculated between Sentinel-1 σ^0 and calibrated WCM simulations. The analysis of the parameters was restricted to the cropland area as no difference between our experiment lines exists over other land cover types (i.e., the irrigation module is active only over grid points classified as crop).

3 RESULTS

3.1 Noah MP regional evaluation

Figure 4 shows maps of the Pearson-R between bi-weekly Noah-MP SSM *Natural* and *Irrigation* simulations and bi-weekly ASCAT and SMAP L2 SSM retrievals, respectively, for April 2015 to December 2019. The Noah-MP SSM *Irrigation* run provides a higher agreement with both satellite SSM data sets compared to the *Natural* run. Indeed, the median Pearson-R between SMAP L2 SSM and Noah-MP SSM increases from 0.68 to 0.73, for the *Natural* run (Figure 4a) and the *Irrigation* run (Figure 4b), respectively. A similar improvement can be observed considering the ASCAT reference SSM, with an improvement in the median Pearson-R of 0.08 when irrigation is activated in the model (from 0.7 to 0.78; Figure 4e). Areas characterized by higher correlation when irrigation is simulated are represented in blue in the Pearson correlation difference map of Figure 4f (obtained by subtracting the map in Figure 4d from the map in Figure 4e). Almost all cropland areas are

characterized by a higher agreement between observations and simulations for the *Irrigation run*. Note that for the evaluation of Noah-MP against SMAP, we relaxed retrieval quality flags, which would otherwise mask out almost the entire study area. The Supplementary material (Figure S2) shows the coverage when using the recommended quality flags. Results in Figure 4 were confirmed by analyzing the RMSE between satellite SSM products and Noah-MP simulations for both the *Natural* and *Irrigation* runs, after rescaling them based on their mean and standard deviation, because SSM retrievals and SSM simulations do not have the same units. Results are displayed in Figure S3 of the Supplementary material and show, for both the satellite products, a general reduction in RMSE when compared with the *Irrigation* run. An improvement in performances can be observed over the entire cropland area, in particular over the central triangle feature where sandy-loam soil texture is present and where, consequently, more irrigation is simulated in the model due to the higher permeability of the soil.

The evaluation of the LAI simulation was limited to the regional scale analysis due to a lack of in situ vegetation data over the selected test sites. The comparison between dekadal values of Noah-MP LAI, from both model runs, and the PROBA-V LAI product was carried out over the reference period January 2015 to October 2019 using the temporal Pearson-R and the ratio bias, shown in Figure 5.

Figure 5a and 5b show that the Pearson-R for vegetation has a lower median value of 0.67 when irrigation is simulated in Noah-MP, whereas this value equals 0.72 for the *Natural* run. The difference between the two Pearson-R maps is shown in Figure 5c, providing evidence of the areas facing a deterioration of the performance in terms of Pearson-R related to the *Irrigation* run. This deterioration is particularly strong over cropland areas south to the Po river (red colour) while the northern area also shows grid cells where the performance improves (blue colour).

By contrast, the ratio bias evaluation score (Figures 5d, 5e, 5f) highlights an improvement in long-term mean vegetation simulations when irrigation is included (Figure 5e). Here the optimal condition is represented by a ratio bias equal to 1 when the mean of the simulated LAI is equal to the mean of the observed LAI. In this context, Figure 5d displays ratio bias values lower than one over a large central triangle-shaped cropland area and median ratio bias value of 0.73, highlighting an underestimation of the LAI simulation related to the *Natural* run. Conversely, Figure 5e shows ratio bias values close to one when irrigation is simulated over an extended cropland area and a median bias value of 0.99. The improvement given by the *Irrigation* run is emphasized in Figure 5f where the histograms of the ratio bias distributions related to both model runs show the higher performance of the *Irrigation* run (red) compared to the *Natural* run (blue) for which the distribution is more skewed to the zero value.

3.2 Noah MP site evaluation

The Noah-MP SSM was evaluated at the Budrio test site field 2 (Figure 1a), using the daily reference PGR SM for the year 2017. Comparisons between the SSM simulations of the *Natural* and *Irrigation* runs with in situ PGR SM are shown in Figure 6a, while daily observed irrigation and rainfall data are compared with daily irrigation simulations in Figure 6b. Soil moisture data are plotted at their original temporal resolution (i.e., daily) to illustrate an issue related to the irrigation timing: SSM simulations in Figure 6a show the ability of the sprinkler irrigation scheme to simulate irrigation in the summer season, but

there is an inevitable problem in reproducing the correct timing and magnitude of irrigation. Indeed, the total amount of simulated irrigation is 604 mm for the 2017 summer season, which overestimates the total amount of observed irrigation, being 349.5 mm. Furthermore, the model simulations not only miss irrigation, but also suffer from erroneous precipitation input, such as on the 11th of July 2017, where the observed precipitation event in the growing season is not found in the model SSM simulations. In any case, bi-weekly Pearson-R between simulated SSM and in situ PGR SM are higher for the *Irrigation* run than for the *Natural* run (0.54 vs 0.42) suggesting the benefit in activating irrigation.

For the Budrio field 1 test site (Figure 1a), two summer seasons of irrigation data were available. To assess the irrigation information contained in Sentinel-1 σ^0 observations (and the potential added value for a forthcoming DA experiment) we compared bi-weekly values of Sentinel-1 σ^0 VV and VH with SSM estimates from both the *Natural* run and *Irrigation* run (Figure 7a) for this site. Although the σ^0 VV is generally used to retrieve SSM (Wagner et al., 2013; Gruber et al., 2013; Bauer-Marschallinger et al., 2018), data at both polarizations were analyzed in order to understand the soil contribution contained in the two signals. Information related to the irrigation periods are shown in Figure 7c, where irrigation observations and irrigation simulations from Noah-MP are compared. Figure 7a indicates that the SSM simulations are better reflected in the Sentinel-1 σ^0 VV than σ^0 VH data, particularly when irrigation is simulated (orange line). The SSM estimates from the *Natural* run (light blue line) agree poorly with the Sentinel-1 data, with Pearson-R values equal to 0.32 and -0.1 for the σ^0 VV (blue dots) and σ^0 VH (cyan dots), respectively. When irrigation is simulated, the σ^0 VV data better follow the modelled SSM signal (Pearson-R of 0.53) especially during the summer irrigation season when the backscatter signal remains higher and stable. On the other hand, σ^0 VH seems to provide poor performances also when irrigation is simulated, with a Pearson-R value equal to 0.06, confirming findings by Baghdadi et al. (2017) which highlighted how the use of VH alone to retrieve SSM is suboptimal when vegetation cover is well developed.

In Figure 7b, the Sentinel-1 σ^0 CR (VH/VV) is compared with Noah-MP LAI from the *Natural* run (light-blue line) and *Irrigation* run (orange line). The performance in terms of Pearson-R decreases from 0.76 to 0.65, when the irrigation is simulated. This is due to a time shift of the Noah-MP LAI growing season in the *Irrigation* run. PROBA-V LAI (in green) was additionally compared with the Sentinel-1 CR (blue dots) showing a Pearson-R of 0.84. The higher agreement between the RS products (Sentinel-1 and PROBA-V) highlights the strong relation between the σ^0 CR and the vegetation signal, suggesting a potential benefit of Sentinel-1 assimilation to correct the simulated vegetation phenology.

Finally, Figure 7c shows a comparison between 15-days accumulated mm of simulated irrigation (in orange) and observed irrigation (in green). The Pearson-R is equal to 0.77, indicating that the sprinkler irrigation scheme can provide acceptable irrigation estimates at this temporal resolution though absolute irrigation amounts are overestimated.

3.3 WCM calibration

The WCM parameters A and B (vegetation parameters), and C and D (soil parameters) were calibrated for each grid cell separately during the reference period January 2017 to December 2019 (Figure 3), using daily σ^0 simulations and observations. The calibrated parameters related to the entire study area for each of the eight experiments are shown in Figure 8 where the

blue left parts of the violin plots identify experiments of the *Natural* run, while the orange right parts of the violin plots are related to the *Irrigation* run.

Generally, the *J*-calibration provides parameter distributions closer around their prior guess as compared to the *KGE*-calibration for which the distributions are often multimodal, especially for the C and D parameters (i.e., Figure 8d, 8h). This is due to the prior parameter penalty, which is included in the Bayesian solution but not in the *KGE*. In general, the calibration of the two functions using the *Natural* run provides wider distributions between lower and upper boundaries for the A vegetation parameter with a high number of grid cells characterized by A-values higher than 0.1 (see *KGE-VV Natural* and *J-VV Natural* experiments in Figures 8a and 8e respectively). Conversely, the *Irrigation* run provides A distributions more skewed to the lower boundary (being also the guess value in each calibration experiment), with a smaller number of grid cells characterized by high A values compared to the *Natural* run. In a preliminary sensitivity study (not shown), we observed that high values of the vegetation parameters A and B, as obtained for the *Natural* run, have the tendency to generate high peaks in the simulated σ^0 during the growing season. Indeed, in the summer, the SSM *Natural* signal is low and not consistent with the Sentinel-1 σ^0, which observes irrigation. In order to follow the temporal dynamics of the Sentinel-1σ^0, the calibration algorithms attribute a relatively higher weight (higher A values) to the LAI than to SSM to compensate for the underestimated SSM in the *Natural* run. By contrast, the *Irrigation* run provides vegetation parameter distributions more skewed to the lower boundaries (see also Section 3.4.2). The C and D parameter distributions feature a better sensitivity to soil moisture dynamics using the *Irrigation* run input data, which is the expected behaviour considering that they describe the σ^0_{soil}. This is true especially when using the *J* cost function (see parameters distributions for the *J-VV Natural* and for the *J-VV Irrigation* experiments in Figures 8g and 8h), which results in more spread in the calibrated C and D distributions for the *Irrigation* simulations (especially in VV polarization), whereas the mode of the C and D parameter distributions for the *Natural* experiments is more shifted to the upper and lower boundaries, respectively.

Figure 9 shows the spatial pattern of the parameters over the study area to better understand the differences between the *Natural* and *Irrigation* calibration runs. We found a connection between the WCM parameters distribution and model parameters, in particular with the HWSD soil texture map (shown in Figure 2). For both the *J-VV Natural* and *J-VV Irrigation* experiments, the activation of the irrigation scheme reduces the dependency of the vegetation-related parameters A and B on soil texture (Figures 9a-b for the *J-VV Natural* and Figures 9e-f for the *J-VV Irrigation* experiment). This is also shown in the parameter maps of the *KGE* calibration experiments (Figure S5 in the Supplementary material). Additionally, the activation of the irrigation scheme, more realistically, shifts the soil texture dependency towards the soil parameters C and D (Figures 9g and 9h), highlighting another important reason for simulating irrigation.

Finally, the different polarization experiments generally provided similar distributions for the vegetation A and B parameters and the D soil parameter. The largest differences between the VV and VH polarizations are identified for the C parameter distributions. This is due to the lower σ^0 signal associated with the VH polarization. Indeed, Figure 8c and 8g are characterized by higher values of the C in VV polarization, as compared to the distributions for VH polarization in Figures 8k and 8o. In the

latter, the C-VH distributions are generally more skewed to the lower boundary of the parameters, with median values closer to the defined guess parameter value.

3.4 WCM evaluation

3.4.1 Regional evaluation

The regional evaluation of the calibration experiments was carried out during the period January 2015 to December 2016 for agricultural areas within the study domain (almost 15,000 km^2), by comparing bi-weekly σ^0 simulations with Sentinel-1 σ^0 in terms of Pearson-R, KGE, and bias. The distribution of the evaluation metrics for the eight experiments is shown in Figure 10. A comparison of the metrics for the *Irrigation* and *Natural* runs confirms better results when irrigation is activated, with violin plots skewed towards more positive values for both KGE and Pearson-R. When stratified by the cost function, the Pearson-R distribution in Figure 10a-d indicates slightly higher performance for the *KGE* (Figures 10a and 10c) than for *J* (Figure 10b and 10d). In terms of the KGE score, simulations are naturally closer to the observations when the *KGE* cost function is used. On the other hand, in terms of bias, generally better performances are found when the Bayesian solution is used (Figures 10i-l). The latter is particularly evident for the VH polarization when comparing the *KGE-VH* and *J-VH* experiments (Figure 10k and 10l).

The VH simulations exhibit a better performance in the *Irrigation* run than VV simulations (Figure 10c-d and Figure 10a-b). Indeed, considering all the statistical scores, the VV polarization is characterized by more similar distributions between the *Natural* and *Irrigation* run for both cost functions. This suggests a higher sensitivity of the VH polarization to the change of vegetation introduced by irrigation, confirming the Sentinel-1 σ^0 VH to be strongly influenced by irrigation as witnessed by the larger score improvement obtained for the calibration experiments *KGE-VH Irrigation* (Figure 10g) and *J-VH Irrigation* (Figure 10h), compared to the *Natural* runs experiments.

In summary, i) VH polarization is more sensitive to the change in the cost function and input data (*Irrigation* or *Natural* run) than VV polarization likely due to its higher sensitivity to vegetation change (Vreugdenhil et al., 2018; Macelloni et al. 2001) which, in the area, is related to the crop development after irrigation, ii) the combination of *J* with activation of the irrigation scheme is able to provide the best unbiased estimates of simulated σ^0 for both VV and VH (*J-VV Irrigation* and *J-VH irrigation* experiments) at the price of generally lower correlations (compared to the *KGE* cost function). This is, however, beneficial for DA as it minimizes the chance of potential error cross correlation between model estimates and observations. Indeed, the match of the temporal dynamic of the signals induced by the correlation term is stronger in the *KGE* than in *J*, which additionally includes a parameter constraint. The higher weight of the correlation in the *KGE* cost function can negatively impact the parameter calibration even when irrigation is turned on in Noah-MP because the simulated irrigation applications are in general not temporally consistent with those seen by Sentinel-1 (see Figure 6).

3.4.2 In situ evaluation

The WCM simulations are further analysed in detail at the Faenza test site (specifically for the San Silvestro field), because it has a larger extent than the Budrio site (see Figure 1), although the same overall conclusions were found for Budrio. Figure 11 shows simulated and observed σ^0 time series for the different experiments highlighted in Figure 3, and Table 2 summarizes the statistics (i.e., Pearson-R, KGE and bias) of each experiment.

The agreement between simulated and observed σ^0 measured by the Pearson-R and KGE in Table 2 generally gives better performances after calibration with the *KGE* cost function than with the *J* cost function. An example is in the higher correlations found for the *KGE-VH Irrigation* experiment as compared to the *J-VH Irrigation* (Figures 11b and 11d respectively). On the other hand, in terms of bias the cost function *J* significantly outperforms the calibration with *KGE* in all experiments with surprisingly comparable values between *Natural* and *Irrigation* runs *(*Table 2*)*.

One undesirable feature of *Natural* runs is the presence of high σ^0 peaks during the summer, clearly detectable over the Faenza test site, especially in the VH polarization, which are less evident in the *Irrigation* run *(*see Figure 11b and 11d). A similar behaviour was found for Budrio (not shown). These peaks are likely attributed to the poor estimation of model vegetation parameter values, previously discussed in section 3.3, when the WCM attempts to compensate for bias in SSM and vegetation input, i.e., input that is not consistent with observations over irrigated areas. This is particularly true for the *KGE* calibration, which does not use a prior parameter constraint. In contrast, the *J* calibration still provides reasonable σ^0 simulations that are closer to the ones of the *Irrigation* run due to the Bayesian technique itself.

Table 2: Results of the site WCM evaluation considering the test site Faenza San Silvestro for each WCM experiment

	KGE-VV *Natural*	*KGE-VV* *Irrigation*	*J-VV* *Natural*	*J-VV* *Irrigation*	*KGE-VH* *Natural*	*KGE-VH* *Irrigation*	*J-VH* *Natural*	*J-VH* *Irrigation*
Pearson-R [-]	0.14	0.27	0.14	0.18	0.33	0.41	0.22	0.38
KGE [-]	0.12	0.26	0.12	0.03	0.20	0.38	0.22	0.31
Bias [dB]	-0.46	-0.55	0.07	0.09	-0.82	0.38	-0.22	-0.02

4 DISCUSSION

4.1 Noah-MP irrigation modelling

The Noah-MP LSM, used as input for the WCM calibration, was evaluated in two configurations, either with a sprinkler irrigation scheme activated or without irrigation (i.e., *Irrigation* run and *Natural* run). Although not all of the Po river valley

is irrigated by sprinkler systems, it most likely still leads to more realistic LSM simulations than not considering irrigation at all.

The main limitation found in the irrigation simulations was related to the irrigation timing and magnitude that was inconsistent with observations. Although this finding is based on only a single study site, it is very likely that it is a widespread issue within the study area for several reasons. In LSMs, the irrigation application is driven by the RZSM availability and consequently by the soil type and the rooting depth parametrizations. Moreover, it is also influenced by the accuracy of the meteorological forcings (especially precipitation, Reichle et al. 2017) which can determine errors in the soil moisture representation. The main reason, however, is likely that irrigation is often the result of subjective farmer decisions rather than objective rules based on the soil state and crop conditions. In theory, the irrigation timing issue could be partly solved by using temporally consistent high-resolution crop maps which should provide a more realistic information of crop phenology and rooting depth. However, in practice, this is unfeasible over many areas of the world given the absence of this information on a large scale. Also, given that irrigation applications are mainly linked to unmodelled processes like rotation schedules for farmers to withdraw water, the correct simulation of the timing can be unsolvable when using models only.

Despite the potential problems related to the unrealistic assumptions in the simulation of irrigation, our results demonstrated that even the use of simple irrigation schemes within Noah-MP can be beneficial. In the regional evaluation, SSM simulations of the *Natural* and *Irrigation* runs were compared with RS SSM from SMAP and ASCAT (Figure 4) on a bi-weekly temporal scale. For both products, we found large improvements in temporal Pearson-R when irrigation was simulated, confirmed by a decrease in the RMSE values over croplands, suggesting that the activation of irrigation modelling provides more realistic SSM estimates. Our findings further confirm the potential of coarse resolution datasets for providing irrigation-related information over intensively irrigated and relatively large agricultural areas, as was shown by Kumar et al. (2015a).

While the impact of irrigation was clear in terms of SSM, the regional evaluation of the simulated LAI against the PROBA-V-based LAI provided contradicting results. In this case, the Pearson-R analysis suggested a deterioration of the Noah-MP simulated LAI when irrigation was activated over the cropland area. We interpreted this correlation deterioration by the absence of specific information about the crop phenology in the model parameterization. In practice, information about the specific crop type is not available and the rooting depth is the sole parameter controlling water uptake from the soil layers. Additionally, information on sowing and harvest periods are not included in the current version of Noah-MP, while irrigated areas are defined based on a global dataset (Salmon et al., 2013) which can suffer accuracy limitations. Indeed, the absence of annual dynamic information on irrigated fields, the unknown yearly variability of the crop types and the impact of the meteorological conditions in the stakeholders decision process (i.e., sowing) make the simulation of Noah-MP prone to LAI peak shifts, as compared to observations, when irrigation is simulated. Another important aspect affecting LAI simulations is its sensitivity to root zone soil moisture, which might be more difficult to simulate than SSM during the irrigation season due to larger impacts of the soil texture and transpiration processes along with the high frequency of the wetting and drying phases caused by irrigation events. This results in a significant performance deterioration (often worse than LAI simulation not including irrigation which are mainly driven by seasonality, see Figure 7). By contrast, irrigation modeling helps in reducing

619 the bias of the LAI simulated time series, which, in the cropland area, show a significant underestimation when irrigation is

620 not considered.

621 The limitations found in simulating LAI and vegetation by Noah-MP even when irrigation was simulated could potentially be

622 overcome by assimilating Sentinel-1 σ^0 data. To explore this potential, we compared the LAI from both model runs, and from

623 PROBA-V, with the observed Sentinel-1 σ^0 CR (VH/VV), which should provide information about the vegetation dynamics

624 (Vreugdenhil et al. 2018; Vreugdenhil et al. 2020). We found that the correlation between σ^0 CR and LAI from PROBA-V was

625 much higher than that between σ^0 CR and the simulated LAI by Noah-MP (see Figure 7) suggesting that Sentinel-1 σ^0 DA

626 could help in correcting poor LAI model simulations. Additionally, a higher correlation was found between the σ^0 VV

627 observations and the simulated SSM when irrigation was turned on than in the absence of irrigation, suggesting that the

628 assimilation of σ^0 VV could improve SSM where irrigation is poorly or not modelled. On the other hand, considering the low

629 correlation between the VH signal and SSM in presence of vegetation (Baghdadi et al. 2017), and its close relation with

630 vegetation (Ferrazzoli et al., 1992; Macelloni et al., 2001), future data assimilation experiments will investigate the contribution

631 of VH and CR in improving LAI predictions and irrigation quantification.

632 Finally, by-weekly accumulated irrigation estimates in Figure 7 agree well with real irrigation applications, suggesting that the

633 large-scale LSM irrigation scheme is helpful for intensively irrigated areas. On the other hand, the poor soil and crop

634 parameterization along with other unknown parameters related to the irrigation management (e.g., the farmers can apply more

635 water than actually needed) can cause large biases in these irrigation simulations. Again, ingestion of radar backscatter data

636 could correct for unmodelled processes. More specifically, Sentinel-1 σ^0 could correct: (i) for the magnitude and timing of the

637 irrigation simulations; and (ii) for Noah-MP irrigation predictions over not irrigated regions.

638 **4.2 WCM backscatter simulation**

639 The purpose of the presented WCM observation operator calibration and evaluation was to optimize the parameters for the

640 future assimilation of the Sentinel-1 σ^0 VV and VH into Noah-MP. Such an optimization would ideally minimize the long-

641 term bias between the simulated and observed σ^0 signals. This can be achieved by calibrating the observation operator with

642 long-term observed σ^0 prior to data assimilation, but in this process, it is crucial to avoid potential error cross-correlation

643 between model observation predictions and observations. Furthermore, a good observation operator should not already

644 compensate for missing processes in the LSM by accepting effective, but unrealistic, optimized parameters, because it would

645 then lose its physically-based ability to accurately convert misfits between observations and simulations to LSM updates during

646 the data assimilation.

647 One way to avoid parameters compensation for erroneous LSM input into the WCM would be to use observed time series of

648 e.g. LAI. However, LAI products from different sensors have different biases themselves which can add bias to the σ^0

649 simulations, and more importantly, replacing simulated LAI or SSM with external datasets would undermine the possibility of

650 updating these variables in the future assimilation system. Based on that, we performed the WCM calibration considering SSM

651 and LAI model input from two different experiments: a *Natural* run and an *Irrigation* run, as well as two cost functions, a

Bayesian solution J and a KGE solution which resulted in four calibration experiments for each polarization (i.e., eight calibration experiments in total).

The calibration experiments using simulations from the *Natural* run as input showed a limited performance and provided presumably bad vegetation parameter estimates which resulted in unrealistic peaks in the simulated σ^0 during the summer, when driven by higher modelled LAI during this period. The inclusion of the irrigation within Noah-MP was very beneficial for all the calibration experiments helping in reducing the bias and increasing the correlation with Sentinel-1 σ^0 as well as removing the anomalous σ^0 increase during warm periods especially for the KGE-based calibration. This corroborates our initial hypothesis that, over intensively irrigated areas, the simulation of irrigation is a mandatory task for an optimal calibration of the WCM. Irrigation modeling, even if only done approximately and perhaps with inaccurate timing, reduces obvious land surface (soil moisture, vegetation) bias and avoids that the WCM needs to compensate for this bias.

Our results show overall higher performance in terms of KGE and Pearson-R scores for the KGE-based calibration, whereas the long-term bias was better reduced for the J-based calibration, which is beneficial in anticipation of future DA. This is because in the J cost function i) a target accuracy term which takes into account also the Sentinel-1 observations error is present; and, ii) a parameter deviation penalty based on the prior parameters constraints is used, which avoid parameters to largely deviate to their prior values.

In terms of polarization, we found σ^0 VH simulations much more sensitive to the inclusion of the irrigation (vs non inclusion) in Noah-MP, suggesting that observed σ^0 VH might also contain much more information about irrigation (via the influence of the vegetation change due to irrigation) than that contained in σ^0 VV which is normally used for SSM retrieval (Vreugdenhil et al. 2020). We believe that the cause of this is related to a comparatively larger σ^0 of vegetation with respect to that of the soil when the crops are well developed. This was also corroborated by the better agreement between CR and LAI from PROBA-V in one of the study sites mentioned above. Despite this, further investigations are required to confirm this hypothesis and DA will certainly help to test this aspect.

5 CONCLUSIONS

With the specific focus on intensively irrigated land, the main objective of this work was to define the optimal calibration of the WCM as observation operator for the future ingestion of Sentinel-1 backscatter into the Noah-MP LSM via DA. In this context, we additionally aimed at: 1) unveiling strengths and limitations of irrigation simulation in LSMs from the perspective of a calibrating the WCM; 2) identifying the potential irrigation-related information contained in the Sentinel-1 σ^0 observations to improve soil moisture and vegetation states as well as irrigation estimates in a calibrated DA system.

To reach these objectives we coupled the Noah-MP with a sprinkler irrigation scheme within LIS and performed two different simulation experiments, one with and one without irrigation (i.e., *Natural* and *Irrigation* runs). Moreover, we coupled a WCM with Noah-MP and tested different calibration options to prepare for optimal, future, assimilation of σ^0 VV and VH to update both soil moisture and vegetation states.

The main conclusions drawn from our evaluation are as follows:

- Over highly irrigated areas, the simulation of irrigation in LSMs helps to provide better soil moisture and vegetation simulations which can be used with benefit as input for the WCM calibration. However, the performance of the irrigation simulations is limited by the simplistic model parameterization of this human process and the necessity to consider realistic and updated land cover information (e.g., crop types). This results in poor simulations of the irrigation timing and quantities as well as vegetation dynamics.

- The Sentinel-1 σ^0 observations contain useful information about SSM and vegetation over highly irrigated areas. This information can be exploited to overcome LSM deficiencies in simulating soil moisture and vegetation over highly irrigated regions, e.g., when irrigation is unmodeled, or poorly modeled because of uncertainties due to crop types, irrigation timing, and farmer agricultural practices. In particular, there is a high chance that the assimilation of Sentinel-1 σ^0 can help in correcting LAI dynamics.

- The optimal assimilation of Sentinel-1 σ^0 into a LSM must rely upon a well calibrated WCM as observation operator to provide unbiased σ^0 simulations with a minimal chance of having error cross-correlations between model and observations, while ensuring a realistic operator controllability or realistic connection between observed signals and land surface state variables. We demonstrated that calibrating the WCM with inclusion of irrigation modeling consistently led to a better agreement with Sentinel-1 σ^0. The modeling of irrigation in the LSM simulations, even if not done optimally, avoids that the WCM calibration compensates for LSM biases.

- We demonstrated that the WCM calibration with a Bayesian cost function, including a prior parameter constraint, provides the optimal WCM parameters, able to generate the lowest bias in the σ^0 simulations for both VV and VH. Although slightly higher correlations are obtained when using a *KGE* cost function, unbiased estimates are particularly beneficial for DA as this minimizes the chance of potential error cross-correlation between model estimates and observations.

This study improves the understanding of the LSM limitations in simulating irrigation and highlights the information content in Sentinel-1 σ^0 data. A natural follow up of this study is the assimilation of σ^0 observations within Noah-MP which should enforce our tested evidence and provide new insights for a more realistic description of the water and carbon cycles over irrigated areas.

ACKNOWLEDGEMENT

The authors would like to thank the European Space Agency (ESA) for the funding support as part of the IRRIGATION+ project (contract n. 4000129870/20/I-NB). For details please visit https://esairrigationplus.org/. Additional acknowledgements go to the Canale Emiliano Romagnolo (CER; Emilia Romagna, Italy) for providing irrigation data over the irrigated test sites. For the Proximal Gamma Ray soil moisture data at the Budrio test site the Authors would like to thank the Department of Physics and Earth Sciences, University of Ferrara Polo Scientifico e Tecnologico, and in particular Dr. Martina Natali, Dr.

716   Virginia Strati, Dr. Alberi Matteo, Dr. Kassandra Giulia Raptis and Prof. Fabio Mantovani. Additionally, the authors want to

717   acknowledge the Vlaams Supercomputer Centrum (VSC) High Performance Computing (HPC) for providing the

718   computational resources needed to realize this study (https://www.vscentrum.be/). Alexander Gruber has received funding

719   from the Research Foundation Flanders (FWO-1224320N and FWO-1530019N).

720   **References**

721   Copernicus Global Land Service Site. Available online: https://land.copernicus.eu/global/

722   Albergel, C., Munier, S., Bocher, A., Bonan, B., Zheng, Y., Draper, C., Leroux, D.J., Calvet, J.: C. LDAS-Monde Sequential
723   Assimilation of Satellite Derived Observations Applied to the Contiguous US: An ERA-5 Driven Reanalysis of the Land
724   Surface Variables, Remote Sens., 10, 1627, doi:/10.3390/rs10101627, 2018

725   Ambika, A.K., Wardlow, B., Mishra, V.: Remotely sensed high resolution irrigated area mapping in India for 2000 to 2015.
726   Sci. Data 3, 160118, doi: /10.1038/sdata.2016.118, 2016.

727   Arsenault, K. R., Kumar, S. V., Geiger, J. V., Wang, S., Kemp, E., Mocko, D. M., Beaudoing, H. K., Getirana, A., Navari, M.,
728   Li, B., Jacob, J., Wegiel, J., Peters-Lidard, C. D.: The Land surface Data Toolkit (LDT v7.2)—A data fusion environment for
729   land data assimilation systems. Geoscientific Model Development, 11(9), 3605–3621, doi: /10.5194/gmd-11-3605-2018, 2018.

730   Attema, E. P.W., Ulaby, F. T.:Vegetation modelled as a water cloud. Radio Science, 13, 357–364,
731   doi:/10.1029/RS013i002p00357, 1978.

732   Badger, A. M. and Dirmeyer, P. A.: Climate response to Amazon forest replacement by heterogeneous crop cover. Hydrology
733   and Earth System Sciences, 19, 4547–4557. doi:/10.5194/hess-19-4547-2015, 2015.

734   Baghdadi, N., Hajj, M.E., Zribi, M., Bousbih, S: Calibration of the water cloud model at C-band for winter crop fields and
735   grasslands. Remote Sens., 9, 969, doi:/10.3390/rs9090969, 2017.

736   Bai, X. and He, B.: Potential of Dubois model for soil moisture retrieval in prairie areas using SAR and optical data. Int. J.
737   Remote Sens.,36, 5737–5753, doi:/10.1080/01431161.2015.1103920, 2015.

738   Ball, J. T., Woodrow, I. E., and Berry, J. A.: A model predicting stomatal conductance and its contribution to the control of
739   photosynthesis under different environmental conditions, Process in Photosynthesis Research, Vol. 1, edited by: Biggins, J.,
740   221– 234, Martinus Nijhoff, Dordrecht, Netherlands, 1987.

741   Bauer-Marschallinger, B., Freeman, V., Cao, S., Paulik, C., Schaufler, S., Stachl, T., Modanesi, S., Massari, C., Ciabatta, L.,
742   Brocca, L. and Wagner, W.: Toward Global Soil Moisture Monitoring With Sentinel-1: Harnessing Assets and Overcoming
743   Obstacles; IEEE Transactions on Geoscience and Remote Sensing, 57, 520 – 539. doi:10.1109/TGRS.2018.2858004, 2018.

744 Baldoncini, M., Alberi, M., Bottardi, C., Chiarelli, E., Raptis, K.G.C., Strati, V., Mantovani, F.: Biomass water content effect

745 on soil moisture assessment via proximal gamma-ray spectroscopy, Geoderma, 335 (2019), pp. 69-77, doi:

746 /10.1016/j.geoderma.2018.08.012, 2019.

747 Bazzi, H., Baghdadi, N., Ienco, D., ElHajj, M., Zribi, M., Belhouchette, H., Escorihuela,M.J., Demarez, V.: Mapping Irrigated

748 Areas Using Sentinel-1 Time Series in Catalonia, Spain. Remote Sens., 11, 1836, doi:10.3390/rs11151836, 2019.

749 Breña-Naranjo, J. A., Kendall, A. D., Hyndman, D. W.: Improved methods for satellite-based groundwater storage estimates:

750 A decade of monitoring the high plains aquifer from space and ground observations, Geophysical Research Letters, 41(17),

751 6167-6173, doi:/10.1002/2014GL061213, 2014.

752 Bretreger, D., Yeo, In-Y., Hancock, G., Willgoose, G.: Monitoring irrigation using landsat observations and climate data over

753 regional scales in the Murray-Darling Basin. Journal of Hydrology 590, 125356, doi:/10.1016/j.jhydrol.2020.125356, 2020.

754 Brocca, L., Ciabatta, L., Massari, C., Moramarco, T., Hahn, S., Hasenauer, S., Kidd, R., Dorigo, W., Wagner, W., Levizzani,

755 V.: Soil as a natural rain gauge: estimating global rainfall from satellite soil moisture data. Journal of Geophysical Research,

756 119(9), 5128-5141, doi:10.1002/2014JD021489, 2014.

757 Brocca, L., Tarpanelli, A., Filippucci, P., Dorigo, W., Zaussinger, F., Gruber, A., Fernández-Prieto, D.: How much water is

758 used for irrigation? A new approach exploiting coarse resolution satellite soil moisture products, International Journal of

759 Applied Earth Observation and Geoinformation, 73C, 752-766, doi: 10.1016/j.jag.2018.08.023, 2018.

760 Brodzik, M., Billingsley, B., Haran, T., Raup, B., Savoie, M.: EASE-Grid 2.0: Incremental but Significant Improvements for

761 Earth-Gridded Data Sets. International Journal of Geo-Information. 1. 32-45. 10.3390/ijgi1010032, 2012.

762 Brutsaert, W. A.: Evaporation Into the Atmosphere, 299 pp., D. Reidel, Dordrecht, the Netherlands, 1982.

763 Carrera, M. L., Bilodeau, B., Bélair, S., Abrahamowicz, M., Russell, A., Wang, X.: Assimilation of passive L-band microwave

764 brightness temperatures in the Canadian Land Data Assimilation System: Impacts on short-range warm season numerical

765 weather prediction, J. Hydrometeor., 20, 1053–1079, https://doi.org/10.1175/JHM-D-18-0133.1, 2019.

766 Chan, S., Bindlish, R., O'Neill, P. E., Jackson, T., Njoku, E. G., Dunbar, S., Chaubell, J., Piepmeier, J. R., Yueh, S., Entekhabi,

767 D., Colliander, A., Chen, F., Cosh, M., Caldwell, T., Walker, J., Berg, A., McNairn, H., Thibeault, M., Martinez-Fernandez,

768 J., Uldall, F., Seyfried, M., Bosch, D., Starks, P., Collins, C. H., Prueger, J., Van der Velde, R., Asanuma, J., Palecki, M.,

769 Small, E. E., Zreda, M., Calvet, J., Crow, W. T., Kerr, Y.: Development and assessment of the SMAP enhanced passive soil

770 moisture product, Remote Sensing of the Environment, 204, 931–941, https://doi.org/10.1016/j.rse.2017.08.025, 2018

771 Chen, F., Janjic, Z., and Mitchell, K. E.: Impact of atmospheric surface-layer parameterizations in the new land-surface scheme

772 of the NCEP mesoscale Eta model, Boundary Layer Meteorol., 85, 391–421, doi:10.1023/A:1000531001463, 1997.

773   Chen, F., Mitchell, K., Schaake, J., Xue, Y., Pan, H. L., Koren, V., Duan, Q. Y., Ek, M., Betts, A.: Modeling of land surface
774   evaporation by four schemes and comparison with fife observations, J. Geophys. Res.-Atmos., 101, 7251–7268,
775   doi:org/10.1029/95JD02165, 1996.

776   Chen, F. and Dudhia, J.: Coupling an advanced land surface hydrology model with the Penn State-NCAR MM5 modeling
777   system. Part I: Model implementation and sensitivity, Mon. Weather Rev., 129, 569–585, doi: 0.1175/1520-
778   0493(2001)129<0569:CAALSH>2.0.CO;2, 2001.

779   Dari, J., Brocca, L., Quintana-Seguí, P., Escorihuela, M. J., Stefan, V., Morbidelli, R.: Exploiting High-Resolution Remote
780   Sensing Soil Moisture to Estimate Irrigation Water Amounts over a Mediterranean Region, Remote Sensing, 12(16), 2593,
781   doi: /10.3390/rs12162593, 2020.

782   De Lannoy, G.J.M., Reichle, R.H.: Assimilation of SMOS brightness temperatures or soil moisture retrievals into a land
783   surface model Hydrol. Earth Syst. Sci., doi:10.5194/hess-2016-414, 2016.

784   De Lannoy, G.J.M., Reichle, R., Pauwels, V.: Global calibration of the GEOS-5 L-band microwave radiative transfer model
785   over non-frozen land using SMOS observations, Journal of Hydrometeorology, 14, 765–785, doi:/10.1175/JHM-D-12-092.,
786   2013.

787   De Lannoy, G.J.M., Reichle, R.H., Vrugt, J.A.: Uncertainty quantification of GEOS-5 L-band radiative transfer model
788   parameters using Bayesian inference and SMOS observations Remote Sens. Environ., 148, pp. 146-157,
789   doi:/10.1016/j.rse.2014.03.030, 2014.

790   De Roo, R.D., Du, Y., Ulaby, F.T., Dobson, M.C.: A semi-empirical backscattering model at L-band and C-band for a soybean
791   canopy with soil moisture inversion. IEEE Trans. Geosci. Remote Sens., 39, 864–872, doi:10.1109/36.917912, 2001.

792   Dierckx, W., Sterckx, S., Benhadj, I., Livens, S., Duhoux, G.,Van Achteren, T., Francois, M., Mellab, K., Saint, G.: PROBA-
793   V mission for global vegetation monitoring: Standard products and image quality, Int. J. Remote Sens., 35, 2589–2614, doi:
794   10.1080/01431161.2014.883097, 2014.

795   Douglas, E., Beltran-Przekurat, A., Niyogi, D., Pielke Sr, R., Vörösmarty, C.J.: The impact of agricultural intensification and
796   irrigation on land–atmosphere interactions and Indian monsoon precipitation — A mesoscale modeling perspective, Global
797   Planet. Change, 67, 117–128, doi:/10.1016/j.gloplacha.2008.12.007, 2009.

798   El Hajj, M., Baghdadi, N., Zribi, M., Belaud, G., Cheviron, B., Courault, D., Charron, F: Soil moisture retrieval over irrigated
799   grassland using X-band SAR data. Remote Sens. Environ. 176, 202–218, https://doi.org/10.1016/j.rse.2016.01.027, 2016.

800 Ek, M. B., Mitchell, K. E., Lin, Y., Rogers, E., Grunmann, P., Koren, V., Gayno, G., Tarpley, J. D.: Implementation of Noah
801 land surface model advancements in the National Centers for Environmental Prediction operational mesoscale Eta model, J.
802 Geophys. Res., 108(D22), 8851, doi:10.1029/2002JD003296, 2003.

803 Entekhabi, D., Njoku, E. G., O'Neill, P. E., Kellogg, K. H., Crow, W. T., Edelstein, W. N., et al.: The Soil Moisture Active
804 and Passive (SMAP) mission. Proceedings of the IEEE, 98(5), 704–716, doi: 10.1109/JPROC.2010.2043918, 2010.

805 Escorihuela, M.J. and Quintana-Segui, P.: Comparison of remote sensing and simulated soil moisture datasets in Mediterranean
806 landscapes. Remote Sens. Environ. 180, 99–114, doi:10.1016/j.rse.2016.02.046, 2016.

807 Evans, J. P., and Zaitchik, B. F.: Modeling the large-scale water balance impact of different irrigation systems, Water Resour.
808 Res., 44, W08448, doi:10.1029/2007WR006671, 2008.

809 FAO 2006. AQUASTAT online database. Food and Agriculture Organization of the United Nations (FAO), available at:
810 http://www.fao.org/ag/agl/aglw/aquastat/main/index.stm

811 Filippucci, P., Tarpanelli, A., Massari, C., Serafini, A., Strati, V., Alberi, M., Raptis, K.G.C., Mantovani, F., Brocca, L.: Soil
812 moisture as a potential variable for tracking and quantifying irrigation: A case study with proximal gamma-ray spectroscopy
813 data, Adv. Water Resour, 136, 103502, doi: /10.1016/j.advwatres.2019.103502, 2020.

814 Foley, J. A., Ramankutty, N., Brauman, K. A., Cassidy, E. S., Gerber, J. S., Johnston, M., Balzer, C.: Solutions for a cultivated
815 planet, Nature, 478(7369), 337-342, doi:/10.1038/nature10452, 2011.

816 Francois, M., Santandrea, S., Mellab, K., Vrancken, D., Versluys, J.: The PROBA-V mission: The space segment, Int. J.
817 Remote Sens., 35, 2548–2564, doi:/10.1080/01431161.2014.883098, 2014.

818 Fung, A: Microwave Scattering and Emission Models and their Applications. Artech House, Boston, MA, 1994.

819 Gao, Q., Zribi, M., Escorihuela, M., Baghdadi, N., Segui, P.: Irrigation mapping using Sentinel-1 time series at field scale.
820 Remote Sensing, 10(9), 1495, DOI:10.3390/rs10091495, 2018.

821 Gelaro, R., McCarty, W., Suárez, M. J., Todling, R., Molod, A., Takacs, L., Randles, C. A., Darmenov, A., Bosilovich, M. G.,
822 Reichle, R., Wargan, K., Coy, L., Cullather, R., Draper, C., Akella, S., Buchard, V., Conaty, A., da Silva, A. M., Gu, W., Kim,
823 G.-K., Koster, R., Lucchesi, R., Merkova, D., Nielsen, J. E., Partyka, G., Pawson, S., Putman, W., Rienecker, M., Schubert, S.
824 D., Sienkiewicz, M., Zhao, B.:The modern-era retrospective analysis for research and applications, version 2 (MERRA-2),
825 Journal of Climate, 30(14), 5419–5454.doi.org/10.1175/JCLI-D-16-0758.1, 2017.

826 Gupta, H.V., Kling, H., Yilmaz, K.K., Martinez, G.F.: Decomposition of the mean squared error and NSE performance criteria:
827 implications   for   improving   hydrological   modelling,   Journal   of   Hydrology,   377 (1–2), pp.   80-91,
828 doi:/10.1016/j.jhydrol.2009.08.003, 2009.

Gutman, G. and Ignatov, A.: The derivation of the green vegetation fraction from NOAA/AVHRR data for use in numerical weather prediction 720 models, International Journal of remote sensing, 19, 1533–1543, doi:/10.1080/014311698215333, 1998.

H SAF, Algorithm Theoretical Baseline Document (ATBD) Metop ASCAT Surface Soil Moisture Climate Data Record v5 12.5 km sampling (H115) and Extension (H116), v0.1, 2019

Haddeland, I., Skaugen, T., Lettenmaier, D.P.: Hydrologic effects of land and water management in North America and Asia: 1700–1992, Hydrol. Earth Syst. Sci., 11, 1035–1045, doi:/10.5194/hess-11-1035-2007, 2007.

Hansen, M. C., DeFries, R. S., Townshend, J. R., Sohlberg, R.: Global land cover classification at 1 km spatial resolution using a classification tree approach, International journal of remote sensing, 21, 1331–1364, doi:/10.1080/014311600210209, 2000.

El Hajj, M., Baghdadi, N., Zribi, M., Bazzi, H.: Synergic Use of Sentinel-1 and Sentinel-2 Images for Operational Soil Moisture Mapping at High Spatial Resolution over Agricultural Areas. Remote Sens., 9, 1292, doi:/10.3390/rs9121292, 2017.

Hu, X., Shi, L., Zeng, J., Yang, J., Zha, Y., Yao, Y., Cao, G.: Estimation of actual irrigation amount and its impact on groundwater depletion: A case study in the Hebei Plain, China. Journal of Hydrology, in press, doi: 10.1016/j.jhydrol.2016.10.020, 2016.

Jalilvand, E., Tajrishy, M., Hashemi, S.A.G., Brocca, L.: Quantification of irrigation water using remote sensing of soil moisture in a semi-arid region, Remote Sensing of Environment, 231, 111226, doi:/10.1016/j.rse.2019.111226, 2019.

Kennedy, J. and Eberhart, R.: "Particle swarm optimization," Proceedings of ICNN'95 - International Conference on Neural Networks, Perth, WA, Australia, pp. 1942-1948 vol.4, doi: 10.1109/ICNN.1995.488968, 1995.

Kolassa, J., Reichle, R., and Draper, C.: Merging active and passive microwave observations in soil moisture data assimilation, Remote Sens. Environ., 191, 117–130, https://doi.org/10.1016/j.rse.2017.01.015, 2017.

Kumar, S. V., Holmes, T. R., Bindlish, R., de Jeu, R., Peters-Lidard, C.: Assimilation of vegetation optical depth retrievals from passive microwave radiometry, Hydrology and Earth System Sciences, 24(7), 3431– 3450. doi:/10.5194/hess-24-3431-2020, 2020.

Kumar, S.V., Peters-Lidard, C.D., Santanello, J.A., Reichle, R.H., Draper, C.S., Koster, R.D., 2015a. Evaluating the utility of satellite soil moisture retrievals over irrigated areas and the ability of land data assimilation methods to correct for unmodelled processes, Hydrol. Earth Syst. Sci. 19, 4463–4478, doi: 10.5194/hessd-12-5967-2015, 2015a.

Kumar, K., Rao, H.P.S., Arora, M.K.: Study of water cloud model vegetation descriptors in estimating soil moisture in Solani catchment, Hydrol. Process. 29, 2137–2148, doi:/10.1002/hyp.10344, 2015b.

Kumar S.V., Reichle, R.H., Peters-Lidard, C.D.: A land surface data assimilation framework using the land information system: Description and applications, Adv. Water Resour. 31, 1419- 1432, https://doi.org/10.1016/j.advwatres.2008.01.013, 2008.

Lawston, P. M., Santanello, J. A., Zaitchik, B. F., Rodell, M.: Impact of irrigation methods on land surface model spinup and initialization of WRF forecasts, J. Hydrometeorol., 16, 1135– 1154, doi:10.1175/JHM-D-14-0203.1, 2015.

Le Page, M., Jarlan, L., El Hajj, M. M., Zribi, M., Baghdadi, N., Boone, A.: Potential for the Detection of Irrigation Events on Maize Plots Using Sentinel-1 Soil Moisture Products, Remote Sensing, 12(10), 1621, https://doi.org/10.3390/rs12101621, 2020.

Li, J. and Wang, S.: Using SAR-Derived Vegetation Descriptors in a Water Cloud Model to Improve Soil Moisture Retrieval. Remote Sens., 10, 1370, https://doi.org/10.3390/rs10091370, 2018.

Lievens, H., Demuzere, M., Marshall, HP. et al.: Snow depth variability in the Northern Hemisphere mountains observed from space, Nat Commun 10, 4629, doi:/10.1038/s41467-019-12566-y, 2019.

Lievens, H., Reichle, R. H.,Liu, Q., De Lannoy, G. J. M., Dunbar, R. S., Kim, S. B., et al. (2017a) Joint Sentinel-1 and SMAP data assimilation to improve soil moisture estimates, Geophysical Research Letters,44,6145–6153, doi:/10.1002/2017GL073904, 2017a.

Lievens, H., Martens, B., Verhoest, N. E. C., Hahn, S., Reichle, R. H., Miralles, D. G.: Assimilation of global radar backscatter and radiometer brightness temperature observations to improve soil moisture and land evaporation estimates, Remote Sens. Environ., 189, 194–210, doi: 10.1016/j.rse.2016.11.022, 2017b.

Lievens, H., Tomer, S., Bitar, A. A., De Lannoy, G., Drusch, M., Dumedah, G., Hendricks-Franssens, H.-J., Kerr, Y., Pan, M., Roundy, J., Vereecken, H., Walker, J., Wood, E., Verhoest, N., Pauwels, V.: SMOS soil moisture assimilation for improved stream flow simulation in the Murray Darling Basin, Australia, Remote Sens. Environ., 168, 146–162, doi:/10.1016/j.rse.2015.06.025, 2015.

Liu C. and Shi J.: Estimation of vegetation parameters of water cloud model for global soil moisture retrieval using time-series L-Band Aquarius observations, IEEE J. Sel. Top. Appl. Earth Observ. Remote Sens., 9, pp. 5621-5633, doi: 10.1109/JSTARS.2016.2596541, 2016.

Macelloni, G., Paloscia, S., Pampaloni, P., Marliani, F., Gai, M.: The relationship between the backscattering coefficient and the biomass of narrow and broad leaf crops. IEEE Trans. Geosci. Remote Sens., 39, 873–884, doi: 10.1109/36.917914, 2001.

Mahrt, L., Pan, H.-L.: A two-layer model of soil hydrology, Boundary Layer Meteorol., 29,1–20, doi:10.1007/BF00119116, 1984.

Miller, J., Barlage, M., Zeng, X., Wei, H., Mitchell, K.,Tarpley, D.: Sensitivity of the NCEP/Noah land surface model to the MODIS green vegetation fraction data set, Geophysical research letters, 33, doi: /10.1029/2006GL026636, 2006.

Monfreda, C., Ramankutty, N., Foley, J. A.: Farming the planet: 2. Geographic distribution of crop areas, yields, physiological types, and net primary production in the year 2000, Glob. Biogeochem. Cycles 22, GB1022, https://doi.org/10.1029/2007GB002947, 2008.

891 Musolino, D., de Carli, A., Massarutto, A.: Evaluation of socio-economic impact of drought events: the case of Po river basin,
892 European Countryside, 9 (1), pp. 163-176, doi:/10.1515/euco-2017-0010, 2017.

893 Nie, W., Zaitchik, B. F., Rodell, M., Kumar, S. V., Arsenault, K. R., Li, B., & Getirana, A.: Assimilating GRACE into a land
894 surface model in the presence of an irrigation-induced groundwater trend, Water Resources Research, 55, 11,274–11,294.
895 doi:/10.1029/2019wr025363, 2019.

896 Nie, W., Zaitchik, B. F., Rodell, M., Kumar, S. V., Anderson, M. C., & Hain, C.: Groundwater withdrawals under drought:
897 Reconciling GRACE and Land Surface Models in the United States High Plains Aquifer, *Water Resources Research*, 48(3),
898 317, doi:/10.1029/2017WR022178, 2018.

899 Niu, G.-Y. and Yang, Z.-L.: Effects of frozen soil on snowmelt runoff and soil water storage at a continental scale, J.
900 Hydrometeorol., 7, 937–952, doi:10.1175/JHM538.1, 2006.

901 Niu, G.-Y., Yang, Z.-L., Dickinson, R. E., Gulden, L. E., Su, H.: Development of a simple groundwater model for use in
902 climate models and evaluation with Gravity Recovery and Climate Experiment data, J. Geophys. Res., 112, D07103,
903 doi:10.1029/2006JD007522, 2007.

904 Niu, G.Y., et al.: The community Noah land surface model with multiparameterization options (Noah-MP): 1. Model
905 description and evaluation with local-scale measurements, J. Geophys. Res. Atmos., 116, pp. 1-19, 10.1029/2010JD015139,
906 2011.

907 Oh, Y. Quantitative retrieval of soil moisture content and surface roughness from multipolarized radar observations of bare
908 soil surfaces, IEEE Trans. Geosci. Remote Sens., 42, 596–601, doi: 10.1109/TGRS.2003.821065, 2004.

909 O'Neill, P. E., Chan, S., Njoku, E. G., Jackson, T., Bindlish, R., Chaubell, J.: SMAP Enhanced L2 Radiometer Half-Orbit 9
910 km EASE-Grid Soil Moisture, Version 4. Boulder, Colorado USA. NASA National Snow and Ice Data Center Distributed
911 Active Archive Center. doi: /10.5067/Q8J8E3A89923, 2020.

912 Ozdogan, M., Gutman, G.: A new methodology to map irrigated areas using multi-temporal MODIS and ancillary data: An
913 application example in the continental US, Remote Sens. Environ. 112, 3520–3537, doi: /10.1016/j.rse.2008.04.010, 2008.

914 Ozdogan, M., Yang, Y., Allez, G., Cervantes, C.: Remote Sensing of Irrigated Agriculture: Opportunities and Challenges,
915 Remote Sens. 2, 2274–2304. doi:10.3390/rs2092274, 2010a.

916 Ozdogan, M., Rodell, M., Beaudoing, H. K., Toll, D. L.: Simulating the effects of irrigation over the United States in a land
917 surface model based on satellite-derived agricultural data, J. Hydrometeor., 11, 171–184, doi:10.1175/2009JHM1116.1,
918 2010b.

919 Paloscia, S., Pettinato, S., Santi, E., Notarnicola, C., Pasolli, L., Reppucci, A.: Soil moisture mapping using Sentinel-1 images:
920 Algorithm and preliminary validation, Remote Sens. Environ., 134, 234–248, doi:/10.1016/j.rse.2013.02.027, 2013.

921 Peel, M.C., B.L. Finlayson, Mcmahon, T.A.: Updated world map of the Koppen-Geiger climate classification. Hydrol. Earth
922 Syst. Sci. 11, 1633–1644, doi:/10.5194/hess-11-1633-2007,2007.

Po River Watershed Authority: Caratteristiche del bacino del fiume Po e primo esame dell'impatto ambientale delle attività umane sulle risorse idriche, 2006. www.adbpo.it

Qian, Y., Yang, Z., Feng, Z., Liu, Y., Gustafson, W. I., Berg, L. K., Ma, H. Y. (2020). Neglecting irrigation contributes to the simulated summertime warm-and-dry bias in the central United States, npj Clim Atmos Sci 3, 31, doi:/10.1038/s41612-020-00135-w, 2020.

Reichle, R.H., Liu, Q., Koster, R., Crow, W., De Lannoy, G.J.M., Kimball, J., Ardizzone, J., Bosch, D., Colliander, A., Cosh, M., Kolassa, J., Mahanama, S., McNairn, H., Prueger, J., Starks, P., Walker, J.: Version 4 of the SMAP Level-4 Soil Moisture Algorithm and Data Product, Journal of Advances in Modeling Earth Systems, 11, 3106-3130, doi:10.1029/2019MS001729, 2019

Romaguera, M., Krol, M., Salama, M., Su, Z., Hoekstra, A.: Application of a remote sensing method for estimating monthly blue water evapotranspiration in irrigated agriculture, Remote Sens. 6, 10033–10050, doi: /10.3390/rs61010033, 2014.

Salmon, J. M., Friedl, M. A., Frolking, S., Wisser, D.: Global rain-fed, irrigated, and paddy croplands: A new high resolution map derived from remote sensing, crop inventories and climate data, International Journal of Applied Earth Observation and Geoinformation, 38, 321–334, doi:/10.1016/j.jag.2015.01.014 , 2015.

Scheerlinck, K., Pauwels, V. R. N., Vernieuwe, H., De Baets, B.: Calibration of a water and energy balance model: Recursive parameter estimation versus particle swarm, Water Resour. Res., 45, W10422, doi:10.1029/2009WR008051, 2009.

Strati, V., Albéri, M., Anconelli, S., Baldoncini, M., Bittelli, M., Bottardi, C., Chiarelli, E., Fabbri, B., Guidi, V., and Raptis, K. G. C., Solimando, D., Tomei, F., Villani, G., Mantovani, F.: Modelling Soil Water Content in a Tomato Field: Proximal Gamma Ray Spectroscopy and Soil–Crop System Models, Agriculture 8(4), 60.568, doi:/10.3390/agriculture804006, 2018.

Strosser, P., et al., 2012: Gap analysis of the water scarcity and droughts policy in the EU European Commission. European Commission, Tender ENV.D.1/SER/2010/0049, 206.

Verger, A., Baret, F., Weiss, M.: Near real-time vegetation monitoring at global scale, IEEE Journal of Selected Topics in Applied Earth Observations and Remote Sensing, 7, 3473-3481. doi:10.1109/JSTARS.2014.2328632, 2014.

Wagner, W., Hahn, S., Kidd, R., Melzer, T., Bartalis, Z., Hasenauer, S., Figa-Saldaña, J., de Rosnay, P., Jann, A., Schneider, S., Komma, J., Kubu, G., Brugger, K., Aubrecht, C., Züger, J., Gangkofner, U., Kienberger, S., Brocca, L., Wang, Y., Blöschl, G., Eitzinger, J., and Steinnocher, K.: The ASCAT soil moisture product: A review of its specifications, validation results, and emerging applications, Meteorol. Z., 22, 5–33, DOI: 10.1127/0941-2948/2013/0399, 2013.

Veloso, A., Mermoz, S., Bouvet, A., Le Toan, T., Planells, M., Dejoux, J.F., Ceschia, E.: Understanding the temporal behaviour of crops using Sentinel-1 and Sentinel-2-like data for agricultural applications, Remote Sens. Environ., 199, 415–426, doi.:/10.1016/j.rse.2017.07.015, 2017.

Vreugdenhil, M., Wagner, W., Bauer-Marschallinger, B., Pfeil, I., Teubner, I., Rüdiger, C., Strauss, P.: Sensitivity of Sentinel-1 Backscatter to Vegetation Dynamics: An Austrian Case Study. Remote Sens., 10, 1396. doi:/10.3390/rs10091396, 2018.

Vreugdenhil, M., Navacchi, C., Bauer-Marschallinger, B., Hahn, S., Steele-Dunne, S., Pfeil, I., Dorigo, W., Wagner, W.: Sentinel-1 Cross Ratio and Vegetation Optical Depth: A Comparison over Europe, Remote Sens., 12, 3404, doi: /10.3390/rs12203404, 2020.

Zaussinger, F., Dorigo, W., Gruber, A., Tarpanelli, A., Filippucci, P., Brocca, L.: Estimating irrigation water use over the contiguous United States by combining satellite and reanalysis soil moisture data, Hydrology and Earth System Sciences, 23, 897-923, doi:10.5194/hess-23-897-2019, 2019.

Zribi, M., Baghdadi, N., Holah, N., Fafin, O.: New methodology for soil surface moisture estimation and its application to ENVISAT-ASAR multi incidence data inversion, Remote Sens. Environ., 96, 485–496, doi:10.1016/j.rse.2005.04.005, 2005.

Zribi, M., Chahbi, A., Shabou, M., Lili-Chabaane, Z., Duchemin, B., Baghdadi, N., Amri, R., Chehbouni, A.: Soil surface moisture estimation over a semi-arid region using ENVISAT ASAR radar data for soil evaporation evaluation, Hydrol. Earth Syst. Sci., 15, 345–358, doi:10.5194/hess-15-345-2011, 2011.
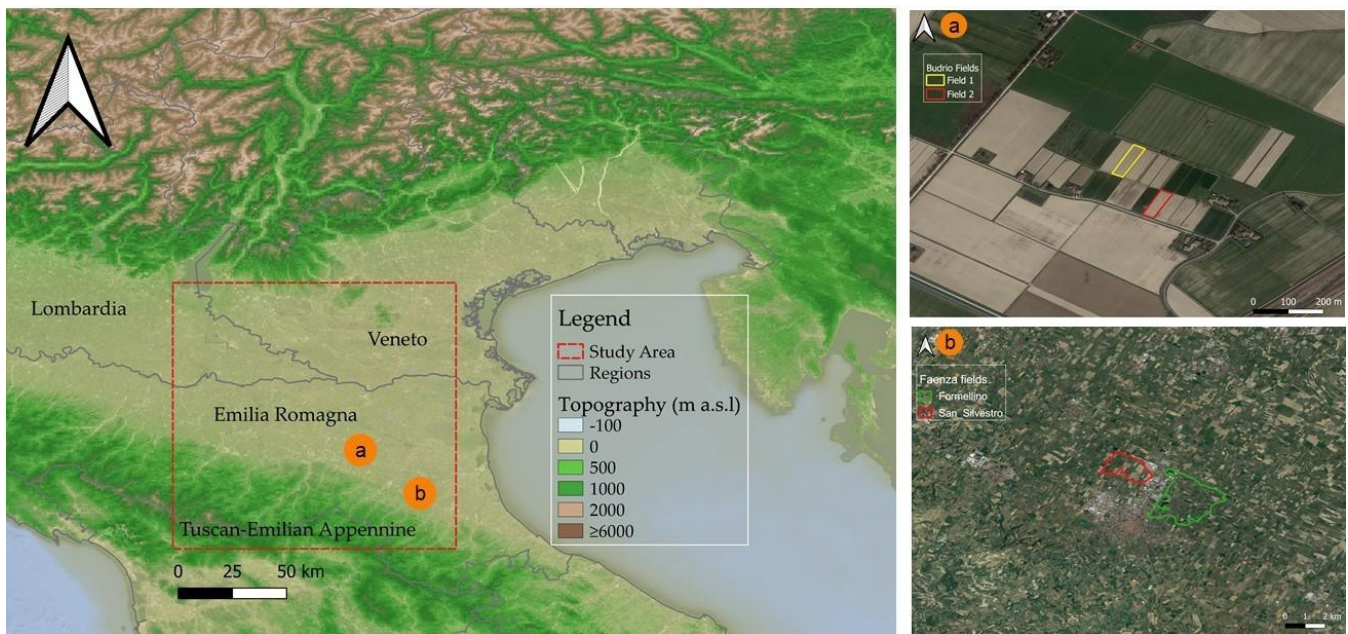
Figure 1: The study area and the two test sites of (a) Budrio and (b) Formellino. Data on the topography are obtained from ETOPO1 Arc-Minute Global Relief Model (Amante & Eakins, 2009). Map data ©2015 Google.

972
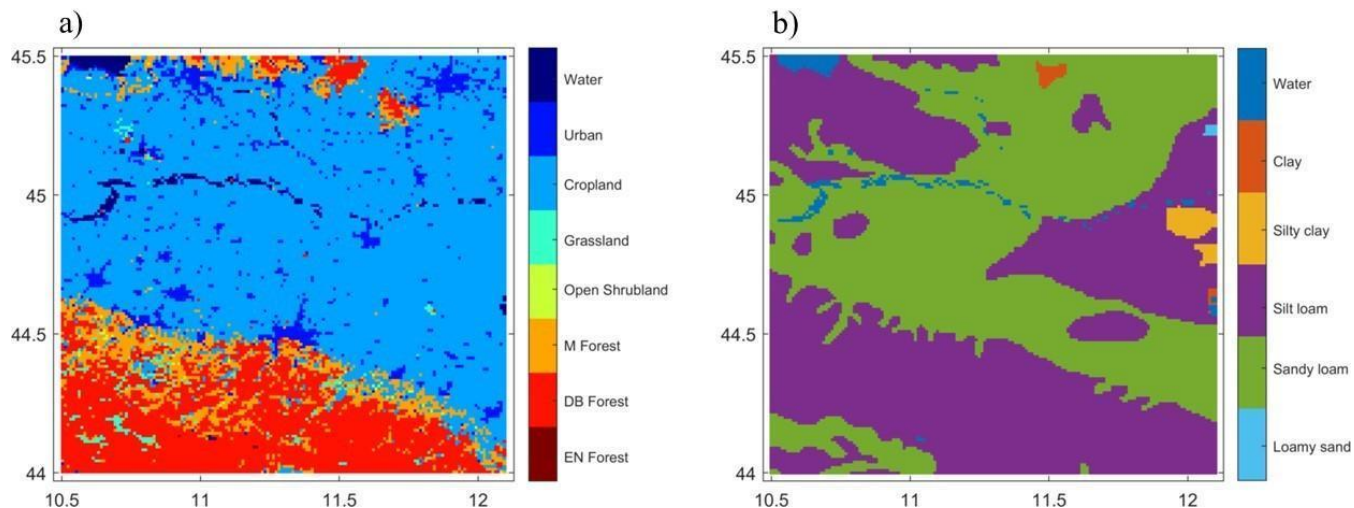
973 **Figure 2: Re-gridded and reclassified input data used in the LIS framework: a) the PROBA-V LC map; and b) the HWSD soil**
974 **texture map.**

975

976
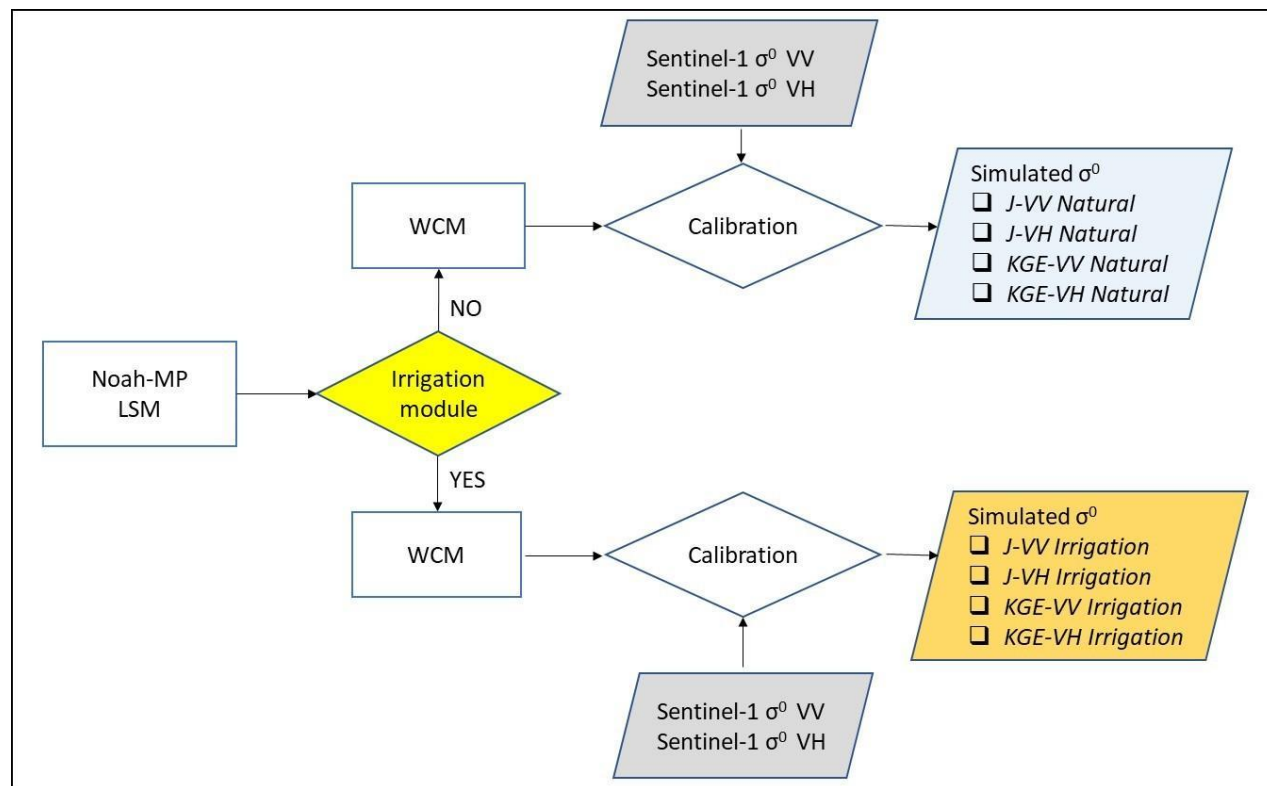
977 **Figure 3**: **Flow chart of the experimental setup used in this study to calibrate the WCM σ^0 signal. A *Natural* and an *Irrigation***
978 **experimental line was performed coupling either Noah-MP *Natural* or *Irrigation* simulations with the WCM. For each experimental**

979 line σ⁰ simulations are driven by the Sentinel-1 signal using two different cost functions (*J* and *KGE*) in order to provide eight
980 different calibration experiments.
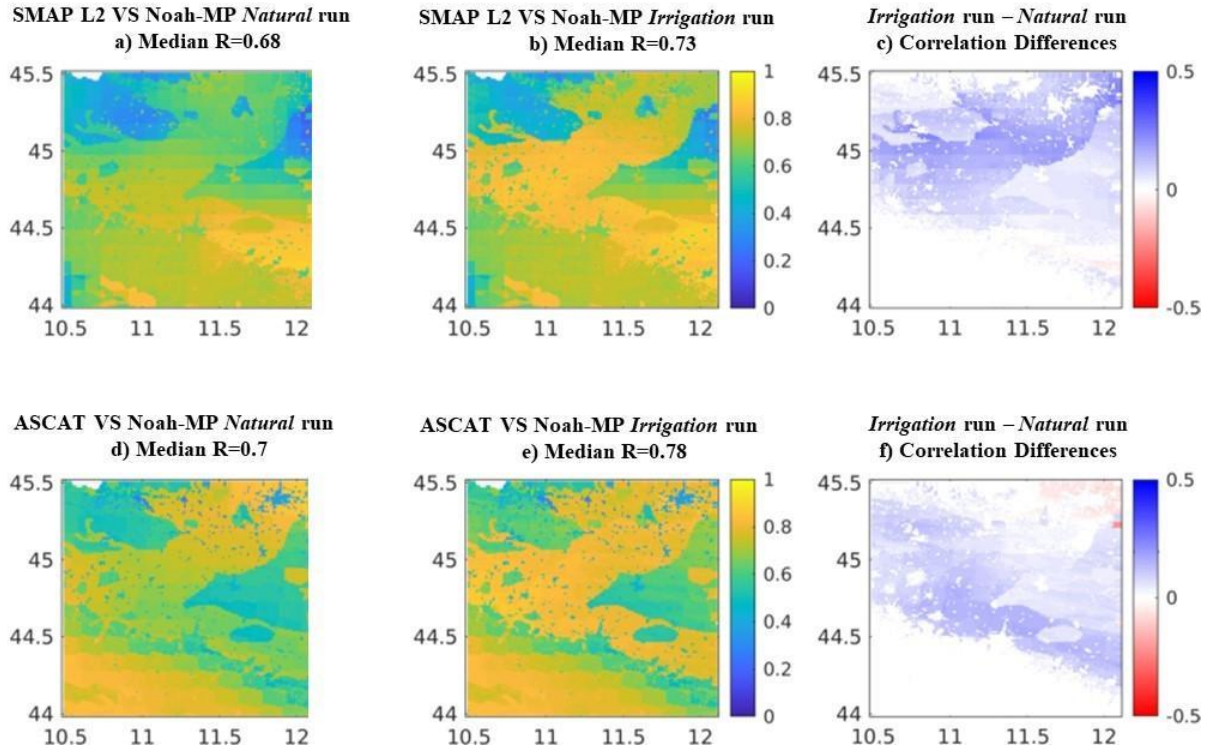
981
982 **Figure 4: Maps of temporal Pearson-R between bi-weekly values of SSM from Noah-MP and satellite retrievals: a)** *Natural* **run and**
983 **SMAP L2; b)** *Irrigation* **run and SMAP L2; d)** *Natural* **run and ASCAT; e)** *Irrigation* **run and ASCAT. Maps of the Pearson-R**
984 **differences display the grid-based difference between: c) map b and map a; f) map e and map d. The reference period is April 2015-**
985 **December 2019.**
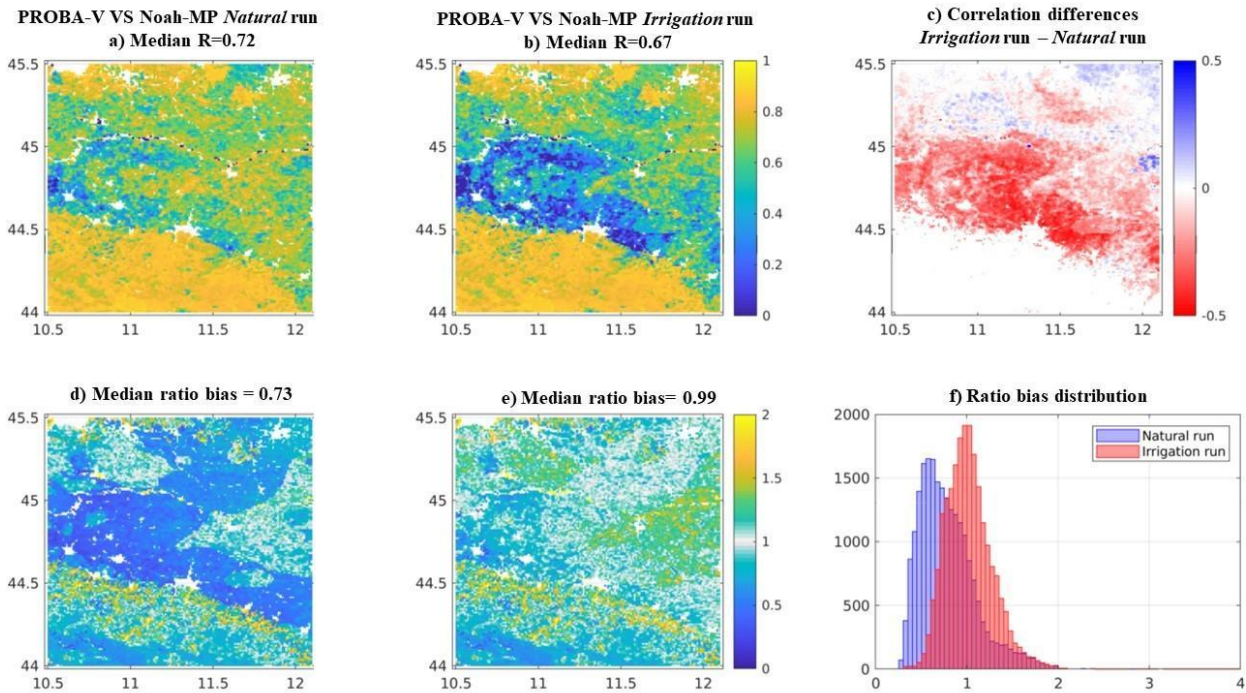
986
987 **Figure 5: Maps of temporal Pearson-R between dekadal LAI values from PROBA-V LAI and Noah-MP LAI: a)** *Natural* **run; b)**
988 *Irrigation* **run. Map of Pearson-R differences between: c) map b and map a. Map of ratio bias of LAI from PROBA-V and Noah-**
989 **MP: d)** *Natural* **run; e)** *Irrigation* **run. Additional histogram distributions from: f) map d and map e. The reference period is January**
990 **2015-October 2019.**
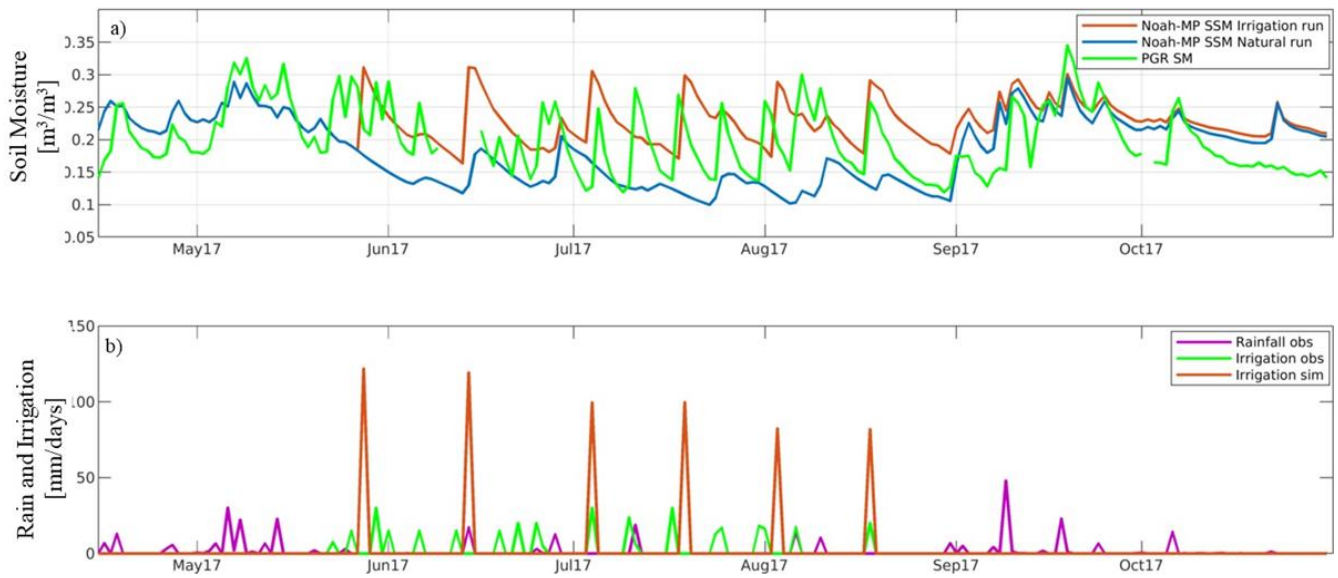
991
992 **Figure 6: Evaluation of SSM over the Budrio field 2, with (green) in situ PGR SM data, (light blue) SSM from Noah-MP** *Natural*
993 **and (orange) SSM from Noah-MP** *Irrigation***. Additional information is provided in the bottom plot: b) observed irrigation (green),**
994 **simulated irrigation (orange) and observed rainfall (magenta) in mm/day**

995
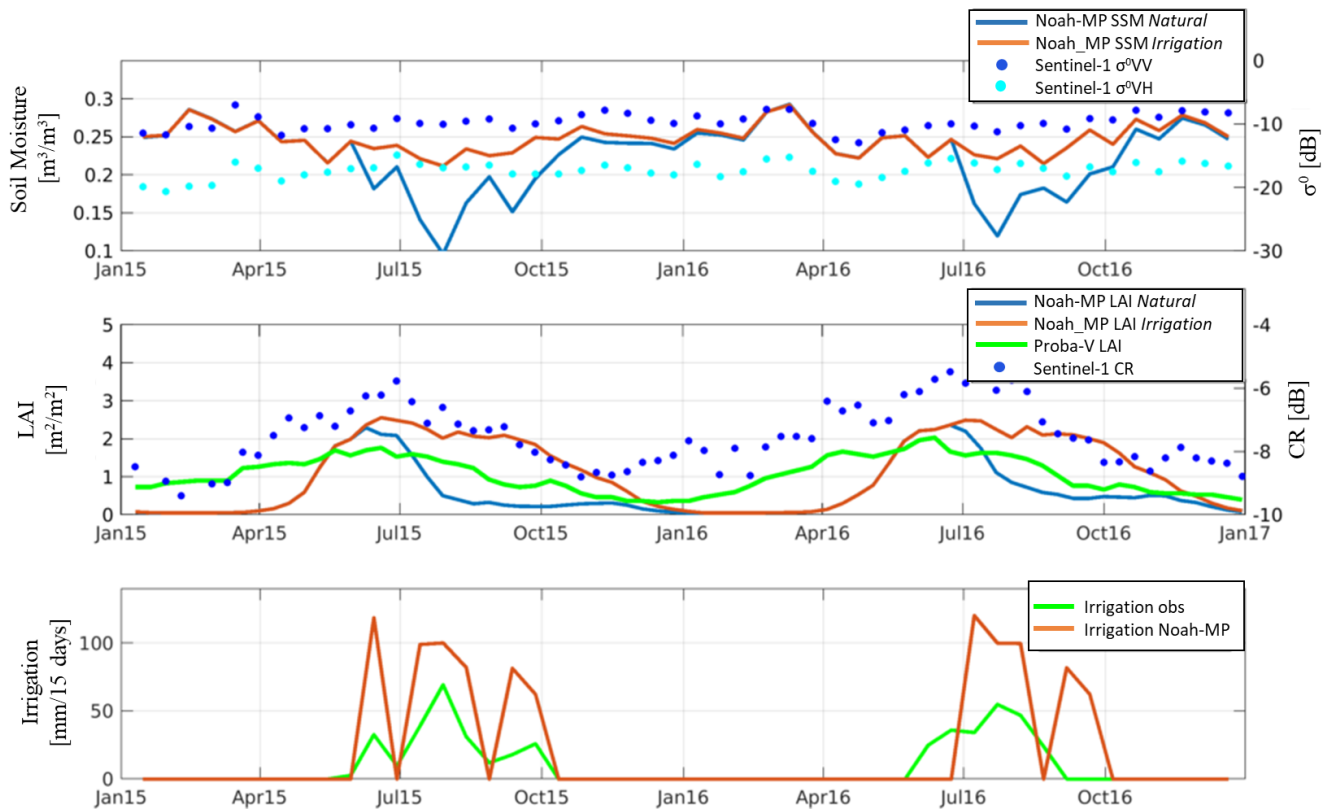
996 **Figure 7: Sentinel-1 σ⁰ VV and VH data for the Budrio field 1 test site compared with Noah-MP SSM, for a)** *Natural* **and** *Irrigation*
997 **runs. Sentinel-1 CR (VH/VV) compared with PROBA-V LAI and Noah-MP LAI for b)** *Natural* **and** *Irrigation* **runs. Also shown are:**
998 **c) observed irrigation (in green) and simulated irrigation from Noah-MP (in orange).**

999
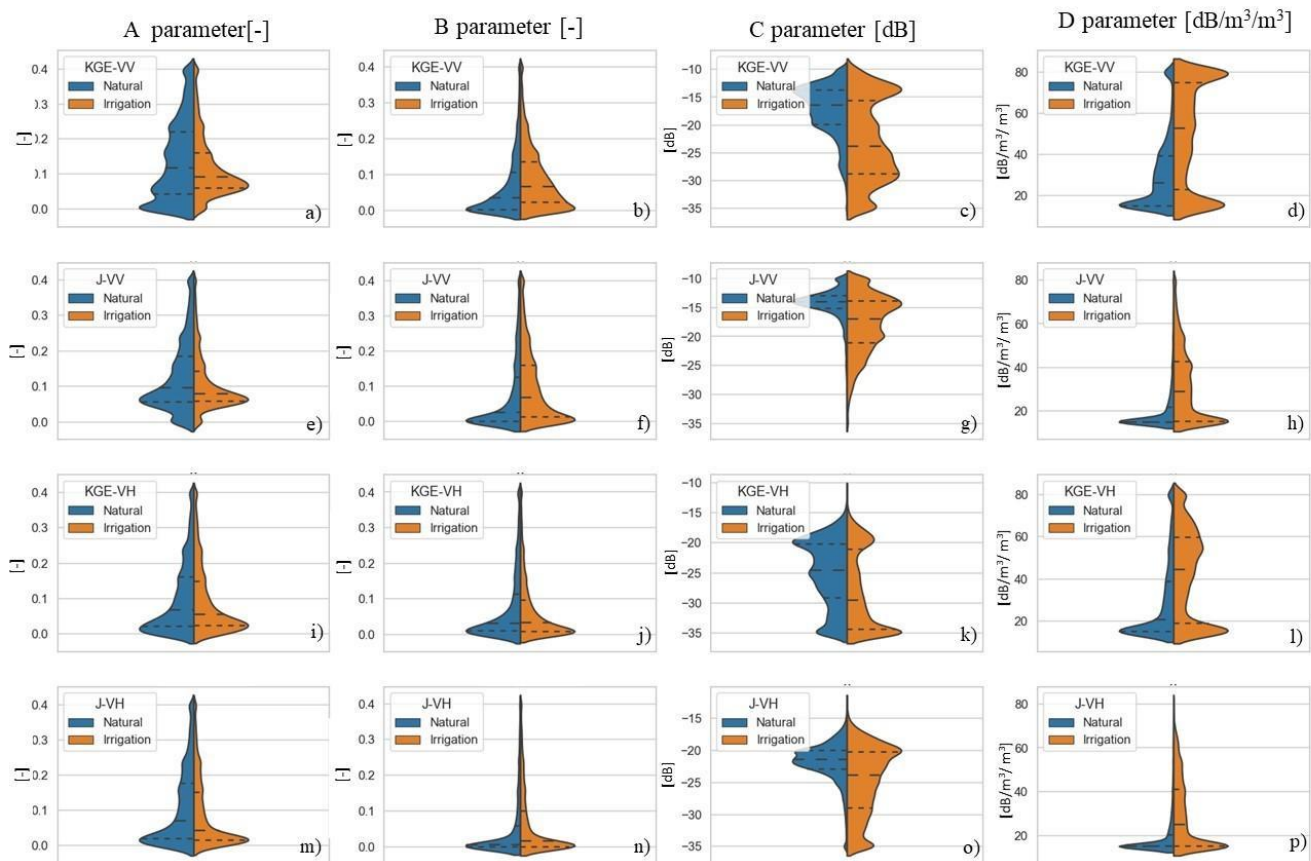
1000 **Figure 8: Split violin distributions of the calibrated parameters over the entire study area for the eight calibration experiments. For**
1001 **both the *Natural* (blue) and *Irrigation* (orange) experiments, the distributions are shown for the A, B, C, and D parameters, (a, b, c,**
1002 **d) using the *KGE* objective function for VV polarization, (e, f, g, h) *J* objective function for VV polarization, (i, j, k, l) *KGE* objective**
1003 **function for VH polarization, and (m, n, o, p) *J* objective function for VH polarization. Note that the areas under the histograms on**
1004 **both left and right sides of the violins are automatically scaled for optimizing the visualization.**

1005

Figure 9. Maps of: a) A parameter; b) B parameter; c) C parameter; d) D parameter for the *J-VV Natural* calibration experiment. Maps of: e) A parameter; f) B parameter; g) C parameter; h) D parameter for the *J-VV Irrigation* calibration experiment.
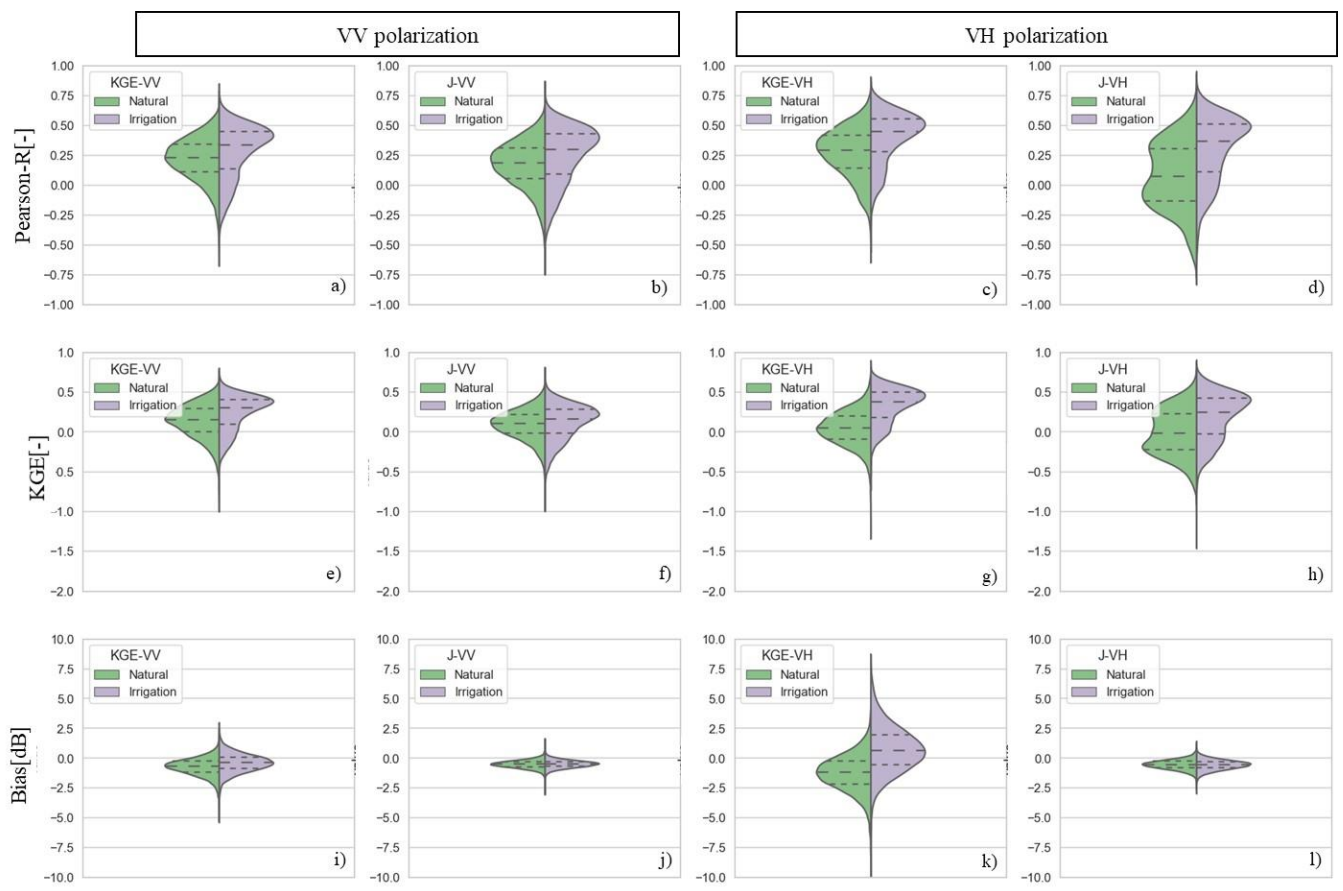
Figure 10: Split violin distributions of (a, b, c, d) Pearson-R, (e, f, g, h) KGE and (i, j, k, l) bias calculated between σ^0 simulations and observations for the validation period, for all the calibration experiments and considering only the cropland areas, using simulations from the *Natural* run (left, green) and the *Irrigation* run (right, violet). The results are shown for VV (first two columns) and VH (right two columns), and alternating for both the calibration with a *J* and *KGE* cost function. Note that the areas under the histograms on both left and right sides of the violins are automatically scaled for optimizing the visualization.

1015
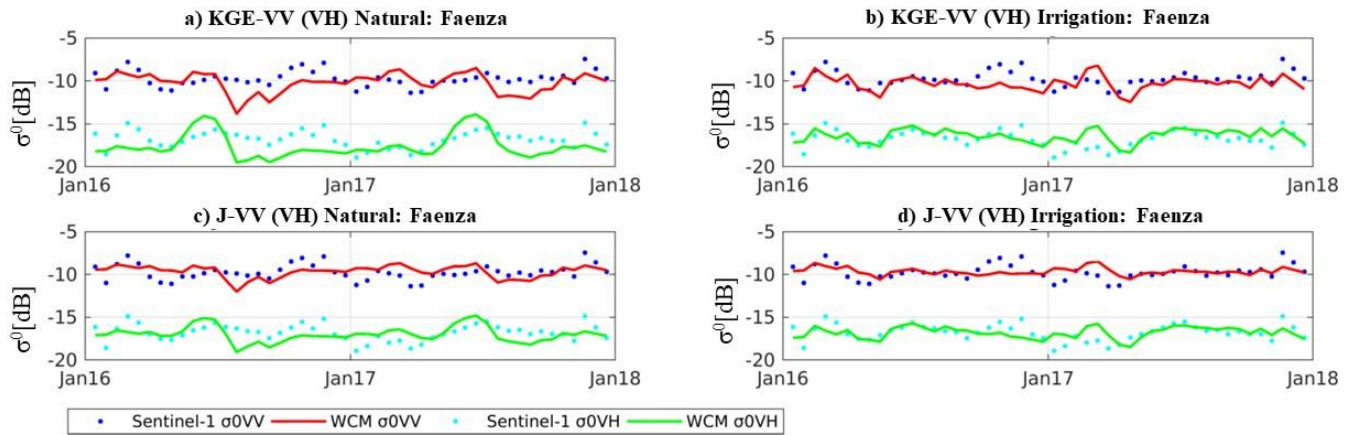
1016 **Figure 11: Comparisons between σ⁰ observations (VV polarization in blue dots and VH polarization light blue dots) and simulations**
1017 **(VV polarization in red and VH polarization in green) in the Faenza San Silvestro field, after calibration with a *KGE* cost function**
1018 **for a) the *Natural* run, b) *Irrigation* run, and after calibration with the *J* cost function for c) the *Natural*, and d) *Irrigation* run.**

1019

1020

1021 **Code and Data availability.**

1022 Data from SMAP can be downloaded at https://nsidc.org/data/SPL2SMP_E/versions/4

1023 Data from ASCAT are available at the website http://hsaf.meteoam.it/

1024 The Sentinel-1 backscatter data processing was done using Google Earth Engine's Python interface and including standard

1025 processing techniques

1026 Data from PROBA-V are available at https://land.copernicus.eu/global/

1027 MERRA-2 data are available at MDISC, managed by the NASA Goddard Earth Sciences (GES) Data and Information Services

1028 Center (DISC, https://disc.gsfc.nasa.gov/datasets?project=MERRA-2)

1029 LIS input and general parameters tables are provided at https://portal.nccs.nasa.gov/lisdata_pub/data/

1030 In situ data are available under request to the original providers.

1031

1032 **Author contributions**: Sara Modanesi designed, coordinated the study and made the analyses. Christian Massari, Gabrielle

1033 De Lannoy and Alexander Gruber designed, coordinated and helped in the data analysis and interpretation. Hans Lievens,

1034 Angelica Tarpanelli and Renato Morbidelli helped in the result interpretation and data processing and collection. All authors

1035 contributed to the editing of the manuscript.

1036

1037 **Competing interests.** The authors declare no competing interest